A Multiplet Analysis of Fe K-Edge 1s → 3d Pre-Edge Features of Iron Complexes

Tami E. Westre,[†] Pierre Kennepohl,[†] Jane G. DeWitt,[†] Britt Hedman,*[,§] Keith O. Hodgson,*[,†,§] and Edward I. Solomon*[,†]

Contribution from the Department of Chemistry and Stanford Synchrotron Radiation Laboratory, Stanford University, Stanford, California 94305

Received December 18, 1996[⊗]

Abstract: X-ray absorption Fe−K edge data on ferrous and ferric model complexes have been studied to establish a detailed understanding of the 1s → 3d pre-edge feature and its sensitivity to the electronic structure of the iron site. The energy position and splitting, and intensity distribution, of the pre-edge feature were found to vary systematically with spin state, oxidation state, geometry, and bridging ligation (for binuclear complexes). A methodology for interpreting the energy splitting and intensity distribution of the 1s → 3d pre-edge features was developed for high-spin ferrous and ferric complexes in octahedral, tetrahedral, and square pyramidal environments and low-spin ferrous and ferric complexes in octahedral environments. In each case, the allowable many-electron excited states were determined using ligand field theory. The energies of the excited states were calculated and compared to the energy splitting in the 1s → 3d pre-edge features. The relative intensities of electric quadrupole transitions into the many-electron excited states were obtained and compared to the intensity pattern of the pre-edge feature. The effects of distorting the octahedral iron site to tetrahedral and square pyramidal geometries were analyzed. The contributions to the pre-edge intensity from both electric quadrupole and electric dipole (from 3d−4p mixing) intensity mechanisms were established for these distorted cases; the amount of 4p character and its distribution over the many-electron final states were experimentally estimated and compared to theoretical predictions from density functional calculations. The methodology was also applied to binuclear complexes, and a clear marker for the presence of a μ-oxo Fe−O−Fe bridge was established. General trends in 3d−4p mixing are developed and discussed for a series of geometries and oxidation states of Fe complexes. The results presented should further aid in the interpretation of the 1s → 3d pre-edge region of iron complexes and non-heme iron enzymes.

Introduction

X-ray absorption spectroscopy (XAS) has been used to investigate the structure of inorganic complexes as well as to characterize iron active sites in both mononuclear and binuclear non-heme iron enzymes.[1−19] While extended X-ray absorption fine structure (EXAFS) analysis provides information on the types of ligating atoms and very accurate first-shell iron−ligand distances, it determines with less accuracy the coordination number and generally gives little or no information on the active site geometry. However, complementary information can be obtained from the edge region of XAS spectra. In particular, the features in the region of the 1s → 3d transition have been shown to be sensitive to the oxidation state and geometry of the iron atom.[20] Additionally, the total intensity of this transition has been shown to increase with decreasing coordination number for iron model complexes due to the loss of inversion symmetry at the iron site.[1,21] Analysis of the 1s → 3d pre-edge feature has already proven useful in the determination of the coordination number of the non-heme iron active sites in ovotransferrin,[1] catechol 1,2-dioxygenase,[1] protocatechuate 3,4-dioxygenase,[1,8] uteroferrin,[11] soybean lipoxygenase,[14,15] rabbit lipoxygenase,[15] human lipoxygenase,[15] bleomycin,[16] and phenylalanine hy-

[†] Department of Chemistry.
[§] Stanford Synchrotron Radiation Laboratory.
[⊗] Abstract published in *Advance ACS Abstracts,* June 1, 1997.

(1) Roe, A. L.; Schneider, D. J.; Mayer, R. J.; Pyrz, J. W.; Widom, J.; Que, L., Jr. *J. Am. Chem. Soc.* **1984**, *106*, 1676.
(2) Kauzlarich, S. M.; Teo, B. K.; Zirino, T.; Burman, S.; Davis, J. C.; Averill, B. A. *Inorg. Chem.* **1986**, *25*, 2781.
(3) Hedman, B.; Co, M. S.; Armstrong, W. H.; Hodgson, K. O.; Lippard, S. J. *Inorg. Chem.* **1986**, *25*, 3708.
(4) Bunker, G.; Petersson, L.; Sjöberg, B.-M.; Sahlin, M.; Chance, M.; Chance, B.; Ehrenberg, A. *Biochemistry* **1987**, *26*, 4708.
(5) Scarrow, R. C.; Maroney, M. J.; Palmer, S. M.; Que, L., Jr.; Roe, A. L.; Salowe, S. P.; Stubbe, J. *J. Am. Chem. Soc.* **1987**, *109*, 7857.
(6) Zhang, K.; Stern, E. A.; Ellis, F.; Sanders-Loehr, J.; Shiemke, A. K. *Biochemistry* **1988**, *27*, 7470.
(7) Tsang, H.-T.; Batie, C. J.; Ballou, D. P.; Penner-Hahn, J. E. *Biochemistry* **1989**, *28*, 7233.
(8) True, A. E.; Orville, A. M.; Pearce, L. L.; Lipscomb, J. D.; Que, L., Jr. *Biochemistry* **1990**, *29*, 10847.
(9) DeWitt, J. G.; Bentsen, J. G.; Rosenzweig, A. C.; Hedman, B.; Green, J.; Pilkington, S.; Papaefthymiou, C. G.; Dalton, H.; Hodgson, K. O.; Lippard, S. J. *J. Am. Chem. Soc.* **1991**, *113*, 9219.
(10) Van der Heijdt, L. M.; Feiters, M. C.; Navaratnam, S.; Nolting, H.-F.; Hermes, C.; Veldink, G. A.; Vliegenthart, J. F. G. *Eur. J. Biochem.* **1992**, *207*, 793.
(11) True, A. E.; Scarrow, R. C.; Randall, C. R.; Holz, R. C.; Que, L., Jr. *J. Am. Chem. Soc.* **1993**, *115*, 4246.
(12) Randall, C. R.; Zang, Y.; True, A. E.; Que, L., Jr.; Charnock, J. M.; Garner, C. D.; Fujishima, Y.; Schofield, C. J.; Baldwin, J. E. *Biochemistry* **1993**, *32*, 6664.
(13) Bertini, I.; Briganti, F.; Mangani, S.; Nolting, H.-F.; Scozzafava, A. *Biochemistry* **1994**, *33*, 10777.
(14) Scarrow, R. C.; Trimitsis, M. G.; Buck, C. P.; Grove, G. N.; Cowling, R. A.; Nelson, M. J. *Biochemistry* **1994**, *33*, 15023.
(15) Pavlosky, M. A.; Zhang, Y.; Westre, T. E.; Gan, Q.-F.; Pavel, E. G.; Campochiaro, C.; Hedman, B.; Hodgson, K. O.; Solomon, E. I. *J. Am. Chem. Soc.* **1995**, *117*, 4316.
(16) Loeb, K. E.; Zaleski, J. M.; Westre, T. E.; Guajardo, R. J.; Mascharak, P. K.; Hedman, B.; Hodgson, K. O.; Solomon, E. I. *J. Am. Chem. Soc.* **1995**, *117*, 4545.
(17) Westre, T. E.; Loeb, K. E.; Zaleski, J. M.; Hedman, B.; Hodgson, K. O.; Solomon, E. I. *J. Am. Chem. Soc.* **1995**, *117*, 1309.
(18) DeWitt, J. G.; Rosenzweig, A. C.; Salifoglou, A.; Hedman, B.; Lippard, S. J.; Hodgson, K. O. *Inorg. Chem.* **1995**, *34*, 2505.
(19) Wang, X.; Randall, C. R.; True, A. E.; Que, L., Jr. *Biochemistry* **1996**, *35*, 13946.
(20) Shulman, R. G.; Yafet, Y.; Eisenberger, P.; Blumberg, W. E. *Proc. Natl. Acad. Sci. U.S.A.* **1976**, *73*, 1384.
(21) Randall, C. R.; Shu, L.; Chiou, Y.-M.; Hagen, K. S.; Ito, M.; Kitajima, N.; Lachicotte, R. J.; Zang, Y.; Que, L., Jr. *Inorg. Chem.* **1995**, *34*, 1036.

S0002-7863(96)04352-1 CCC: $14.00

droxylase.[22] Furthermore, the splitting of the pre-edge feature was used to characterize the oxidation state and spin state of the iron site in activated bleomycin.[17]

XAS edge spectra of first-row transition metals have a weak pre-edge feature ~10 eV below the absorption edge. This feature was assigned as originating from a 1s → 3d transition by Shulman *et al.* when they observed that Zn(II), a d^{10} system, did not display this feature.[20] For complexes in a centrosymmetric environment, a 1s → 3d transition is electric dipole forbidden by parity considerations. However, a very weak pre-edge feature is still experimentally observed for such complexes. Electric quadrupole coupling is the most likely intensity mechanism in such cases. Experimentally, the electric quadrupole nature of the 1s → 3d pre-edge feature in D_{4h} $CuCl_4^{2-}$ was demonstrated by Hahn *et al.* by analysis of the angular dependence of the 1s → 3d transition intensity using polarized synchrotron radiation and oriented single crystals.[23] Theoretically, electric quadrupole coupling has been calculated to be 2 orders of magnitude weaker than electric dipole coupling.[24,25] Complexes in noncentrosymmetric environments have more intense pre-edge features than centrosymmetric complexes.[1,21,23,26−29] This increase in intensity has been attributed to metal 4p mixing into the 3d orbitals which provides some electric dipole allowed 1s → 4p character to the transition, and thus adds to the intensity from the electric quadrupole mechanism. Since the electric quadrupole-coupled mechanism is so much weaker than the electric dipole-coupled mechanism, only a few percent of 4p mixing into the 3d orbitals can have a significant effect on the intensity of the 1s → 3d pre-edge feature.

In this study, XAS Fe−K edge data on high- and low-spin ferrous and ferric inorganic model complexes with varying geometries, as well as binuclear complexes with varying oxidation states, geometries, and oxo *vs* OH^- bridging ligation, have been measured in order to establish a detailed understanding of the energy, intensity, and splitting of the 1s → 3d pre-edge feature and its sensitivity to the electronic and geometric structure of the iron site. The energy splitting and intensity distribution of the pre-edge features of these complexes vary with spin state, oxidation state, geometry, and bridging ligation (in the binuclear complexes). A methodology for interpreting this energy splitting and intensity distribution of the 1s → 3d pre-edge features is developed for high-spin ferrous and ferric complexes in octahedral, tetrahedral, and square pyramidal environments and low-spin ferrous and ferric complexes in octahedral environments. In each case, the allowable many-electron excited states are determined using ligand field theory. The energies of the excited states are calculated and compared to the measured energy splitting in the 1s → 3d pre-edge features. The relative intensities of transitions into the many-electron excited states are obtained and also compared to the observed intensity pattern of the pre-edge feature. Contributions to pre-edge intensities from both electric quadrupole and electric dipole (from 3d−4p mixing) intensity mechanisms are determined experimentally and compared to theoretical estimates of the amount of 4p mixing into specific d orbitals and its distribution over the final states as determined from molecular orbital calculations and ligand field theory. A systematic study of geometric perturbations and their effect on pre-edge spectra is used to evaluate the sensitivity of XAS to geometric and electronic structural changes. Taken together, one derives a coherent interpretation of the 1s → 3d transition in Fe complexes that directly relates to the electronic and geometric structures of the Fe site.

Experimental Section

I. Sample Preparation. FeF_2, $FeCl_2$, $FeBr_2$, FeI_2, $[Fe(H_2O)_6][SiF_6]$, $[Fe(H_2O)_6](NH_4)_2(SO_4)_2$, FeF_3, $FeCl_3$, $FeBr_3$, $Fe(acac)_3$, $[Fe(H_2O)_6](NH_4)(SO_4)_2\cdot 6H_2O$, $K_3[Fe(CN)_6]$, and $K_4[Fe(CN)_6]\cdot 3H_2O$ were purchased from Aldrich in >98% purity and used without further purification. FeF_2, $FeCl_2$, $FeBr_2$, FeI_2, $[Fe(H_2O)_6][SiF_6]$, and $[Fe(H_2O)_6](NH_4)_2(SO_4)_2$ are air-sensitive, and therefore, these complexes were shipped in Ar-filled bottles and immediately placed in an inert atmosphere glovebox upon delivery. All other model complexes were prepared as previously described (see references in Tables 1−3). The crystalline samples were each mixed with boron nitride (BN) and ground into a fine powder. The BN/sample mixture was pressed into a 1 mm thick Al spacer that was sealed with 63.5 μm Mylar tape windows. All air-sensitive complexes were prepared in an inert atmosphere nitrogen-filled glovebox and immediately frozen in liquid nitrogen.

II. XAS Data Collection and Reduction. X-ray absorption spectra were recorded at the Stanford Synchrotron Radiation Laboratory (SSRL) and the National Synchrotron Light Source (NSLS) on beamlines 2-3, 4-2, 4-3, 7-3, and X19A, under ring conditions 3 GeV, 30−100 mA and 2.5 GeV, 100−200 mA, respectively. Tables 1−3 give the respective beamlines and temperatures at which the data were collected for each sample.[30] In all cases, the radiation was monochromatized using a Si(220) double-crystal monochromator. For the majority of the data, the vertical aperature of the pre-monochromator slits was 1 mm. The only exception was for the $[Fe(TMC)X](BF_4)$ series (where $X = Cl^-$, Br^-, CH_3CN^-, and N_3^-) in which case the pre-monochromator slit opening was 1.5 mm vertically. Data were measured in transmission mode with N_2-filled ionization chambers to $k = 9.5$ Å^{-1}, detuning the monochromator 50% at 7474 eV to minimize harmonic contamination (in some cases the data were measured to $k = 15$ Å^{-1} in order to also obtain EXAFS data). In general, two to five scans were measured for each sample. A smooth pre-edge background was removed from each averaged spectrum by fitting a first-order polynomial to the pre-edge region and subtracting this polynomial from the entire spectrum. A two-segment spline of order 2 was fit to the EXAFS region, and all data were normalized to an edge jump of 1 at 7130 eV. Energies were calibrated using an internal Fe foil standard, assigning the first inflection point to 7111.2 eV.[31] The spectrometer energy resolution was approximately 1.4 eV[32] with reproducibility in edge position determination of <0.2 eV.

III. Data Analysis. The intensities and energies of the pre-edge were quantitated by least-squares fits to the data. The fitting program EDG_FIT, which utilizes the double precision version of the public domain MINPAK fitting library[33] was used. EDG_FIT was written

(22) Loeb, K. E.; Westre, T. E.; Kappock, T. J.; Mitic, N.; Glasfeld, J.; Caradonna, J. P.; Hedman, B.; Hodgson, K. O.; Solomon, E. I. *J. Am. Chem. Soc.* **1997**, *119*, 1901.

(23) Hahn, J. E.; Scott, R. A.; Hodgson, K. O.; Doniach, S.; Desjardins, S. R.; Solomon, E. I. *Chem. Phys. Lett.* **1982**, *88*, 595.

(24) Blair, R. A.; Goddard, W. A. *Phys. Rev.* **1980**, *B22*, 2767.

(25) Brouder, C. *J. Phys.: Condens. Matter* **1990**, *2*, 701.

(26) Wong, J.; Lytle, F. W.; Messmer, R. P.; Maylotte, D. H. *Phys. Rev.* **1984**, *B30*, 5596.

(27) Kau, L.-S.; Spira-Solomon, D. J.; Penner-Hahn, J. E.; Hodgson, K. O.; Solomon, E. I. *J. Am. Chem. Soc.* **1987**, *109*, 6433.

(28) Colpas, G. J.; Maroney, M. J.; Bagyinka, C.; Kumar, M.; Willis, W. S.; Suib, S. L.; Baidya, N.; Mascharak, P. K. *Inorg. Chem.* **1991**, *30*, 920.

(29) Sano, M.; Komorita, S.; Yamatera, H. *Inorg. Chem.* **1992**, *31*, 459.

(30) Abbreviations used: acac = acetylacetonate; $BIPhMe_2$ = bis[2-(1-methylimidazolyl)phenyl]methoxymethane; $BzPhMe_2N$ = benzyldimethylphenylammonium; Chel = 4-hydroxo-2,6-pyridinedicarboxylate; Dipic = 2,6-pyridinedicarboxylate; EDTA = ethylenediaminetetraacetic acid; $HB(pz)_3$ = [tri-1-pyrazolylborate]$^-$; $HB(3,5\text{-}iPr_2pz)_3$ = hydrotris(3,5-diisopropyl-1-pyrazolyl)borate; HPTB = [*N*,*N*,*N*′,*N*′-tetrakis(2-benzimidazoylmethyl)-2-hydroxy-1,3-diaminopropane]$^-$; phen = 1,10′-phenanthroline; prpepH = *N*-[2-(4-imidazolyl)ethyl]pyrimidine-4-carboxamide; salen = *N*,*N*′-ethylenebis(salicylideniminato); salmp = [2-[bis(salicylidenamino)methyl]-phenolate]$^{3-}$; TMC = 1,4,8,11-tetramethyl-1,4,8,11-tetraazacyclotetradecane; TPA = tris(2-pyridylmethyl)amine; *OAc* = acetate bridge; *OPh* = phenolate bridge; *OPht* = phthalate bridge; *OBz* = benzoate bridge.

(31) Scott, R. A.; Hahn, J. E.; Doniach, S.; Freeman, H. C.; Hodgson, K. O. *J. Am. Chem. Soc.* **1982**, *104*, 5364.

(32) Lytle, F. W. In *Applications of Synchrotron Radiation*; Winick, H., Xiam, D., Ye, M.-H., Huang, T., Eds.; Gordon and Breach Science Publishers: New York, 1989; p 135.

(33) Garbow, B. S.; Hillstrom, K. E.; More, J. J., Argonne National Laboratory.

by Dr. Graham N. George of SSRL. The pre-edge features were modeled by pseudo-Voigt line shapes (simple sums of Lorentzian and Gaussian functions),[32,34−36] and the energy position, the full width at half-maximum (FWHM) and the peak height were varied. A fixed 50:50 ratio of Lorentzian to Gaussian functions successfully reproduced the spectral features of the pre-edge transitions. Functions modeling the background underneath the pre-edge features were chosen empirically to give the best fit and included a pseudo-Voigt function that mimicked the white line and in some cases additional pseudo-Voigt functions that mimicked shoulders on the rising edge. Furthermore, the second derivative of the data was compared to the second derivative of the fit. For a fit to be deemed acceptable it had to match the data and the second derivative of the data within the noise level. In all cases, a number of acceptable fits, typically eight, were obtained which equally well reproduced the data and the second derivative, varying the energy range over which the data were fit and the background functions used. All spectra were fit over three energy ranges: 7108−7116, 7108−7117, and 7108−7118 eV. Typically, only functions modeling the pre-edge peaks and one function modeling the background were needed to obtain a good match to the data over the range 7108−7116 eV, while functions modeling shoulders on the rising edge were needed to obtain a good match to the data over the range 7108−7118 eV. The value reported for the intensity of a fitted feature (calculated as the peak area, approximated by the height × FWHM) is the average of all the pseudo-Voigt functions that fit the pre-edge features from all the successful fits. To quantitate the error, the standard deviations for the peak energies and intensities were calculated from all the pseudo-Voigt functions that fit the pre-edge features from all the successful fits for each sample.

IV. Density Functional Calculations. Theoretical molecular orbital calculations were based on approximate density functional theory (DFT) using the Amsterdam density functional computational package (ADF, version 2.0.1).[37,38] All DFT calculations were performed using the local density approximation (LDA) parametrization of Vosko, Wilk, and Nussair[39] with nonlocal gradient corrections from Becke[40−42] and Perdew[43,44] added self-consistently. The frozen core approximation was used for all orbitals other than those within the valence shell and above. All valence orbitals were described using a triple-ζ STO basis. Calculations were determined to a final gradient no greater than 10^{-6} au and with a numerical integration precision between 6.0 and 8.0. Orbital contributions to calculated molecular orbitals are reported as Mulliken populations to the nearest 0.1% unless otherwise stated.

Ground state and final state wave functions were calculated for a number of characteristic systems of T_d, C_{4v}, and O_h symmetry. Final states were estimated using relaxed and screened excited state potentials. The iron excited state orbitals were approximated as $Z + 1$ (Co) ground state orbitals to account for the increased effective nuclear charge on the metal center upon promotion of a 1s electron to a 3d orbital. Final state calculations were performed using $d^{(n+1)}$ valence excited electronic configurations. For example, XAS K-edge transitions for $Fe^{III}(d^5)$ species were calculated using $Co^{III}(d^6)$ with appropriate bond lengths for the parent Fe(III) species. This type of methodology has been shown to afford good simulations of XAS final states.[45] The amount of 4p mixing into a particular empty 3d orbital is reported for excited state 4p contributions to the acceptor orbital in the K-edge transition and for the ground state calculations. XAS pre-edge simulations were done by calculating relative final state energies for all single-determinant solutions to final state terms by breaking the symmetry (when necessary) to calculate specific electron occupancies. Relative intensities were calculated from the ground state Fe 3d (quadrupolar) and Fe 4p (dipolar) contributions to the acceptor orbital and weighted as described below.

Results and Analysis

Fe K-edge XAS data were measured for approximately 50 monomeric and dimeric iron model complexes. The energies and intensities of the 1s → 3d pre-edge features were determined as described earlier by fits to the data and are presented in Tables 1 (high-spin iron complexes), 2 (binuclear complexes), and 3 (low-spin iron complexes). A multiplet analysis was employed to evaluate the energy splitting and intensity patterns of the pre-edge features for various cases: high-spin ferrous complexes (O_h, T_d, and C_{4v} geometries), high-spin ferric complexes (O_h, T_d, and C_{4v} geometries), binuclear complexes, and O_h low-spin ferrous and ferric complexes. In each case, the strong field many-electron states were determined for the $d^{(n+1)}$ excited state[90] where the dominant effect of the 1s core hole is an increase in the potential since it is spherically symmetric.[91] The relative energies of the many-electron excited final states were determined by using reasonable values for $10Dq$, B, and C (*vide infra*) and solving the Tanabe−Sugano matrices.[92] Density functional calculations were also used to simulate representative spectra using calculated ligand field parameters. The intensity of the pre-edge features due to the transition into each many-electron state was analyzed in terms of both electric quadrupole and electric dipole intensity mechanisms. The amount of 4p mixing into the 3d orbitals and its distribution over the many-electron final states were estimated from experiment and compared to theoretical estimates from DFT calculations.

I. High-Spin Ferrous Complexes. A. O_h Geometry. Fe K-edge XAS data were measured for high-spin ferrous octahedral model complexes with varying ligation (F^-, Cl^-, Br^-, I^-, H_2O, and imidazole). Of these, FeF_2 is most distorted from O_h symmetry with a 0.1 Å compression of the axial ligands with respect to the equatorial ligands.[46] The other seven complexes have iron sites that are nearly O_h with ligand distances that differ by less than 0.05 Å. The XAS edge spectra for FeF_2, $FeCl_2$, $FeBr_2$, and FeI_2 are shown in Figure 1A, while those for rinneite (Cl^- ligation), $[Fe(H_2O)_6][SiF_6]$, $[Fe(H_2O)_6](NH_4)_2(SO_4)_2$, and $[Fe(imidazole)_6]Cl_2$ are shown in Figure 1B. The lowest energy transitions are the weak 1s → 3d pre-edge peaks at approximately 7112 eV. The 1s → 4p transition occurs at approximately 7125 eV, followed by the near-edge and EXAFS regions dominated by final state single and multiple photoelectron scattering processes. An expanded view of the 1s → 3d pre-edge region is shown as insets in Figure 1A,B. The energies and intensities of the pre-edge features are presented in Table 1. All eight high-spin ferrous octahedral model complexes have two very weak pre-edge features split

(34) Agarwal, B. K. *X-ray Spectroscopy*; Springer-Verlag: Berlin, 1979; p 276.
(35) Lytle, F. W.; Greegor, R. B.; Sandstrom, D. R.; Marques, E. C.; Wong, J.; Spiro, C. L.; Huffman, G. P.; Huggins, F. E. *Nucl. Instrum. Methods* **1984**, *226*, 542.
(36) Tyson, T. A.; Roe, A. L.; Frank, P.; Hodgson, K. O.; Hedman, B. *Phys. Rev.* **1989**, *B39*, 6305.
(37) Baerends, E. J.; Ellis, D. E.; Ros, P. E. *J. Chem. Phys.* **1973**, *2*, 41.
(38) teVelde, G.; Baerends, E. J. *J. Comput. Chem.* **1992**, *99*, 84.
(39) Vosko, S. J.; Wilk, M.; Nussair, M. *Can. J. Phys.* **1980**, *58*, 1200.
(40) Becke, A. *J. Chem. Phys.* **1986**, *84*, 4524.
(41) Becke, A. *J. Chem. Phys.* **1988**, *88*, 1053.
(42) Becke, A. *Phys. Rev.* **1988**, *A38*, 3098.
(43) Perdew, J. P. *Phys. Rev.* **1986**, *B33*, 8822.
(44) Perdew, J. P. *Phys. Rev.* **1986**, *B34*, 7406.
(45) Briois, V.; Cartier dit Moulin, C.; Sainctavit, P.; Brouder, C.; Flank, A.-M. *J. Am. Chem. Soc.* **1995**, *117*, 1019.
(46) Stout, J. W.; Reed, S. A. *J. Am. Chem. Soc.* **1954**, *76*, 5279.
(47) Ferrari, A.; Braibanti, A.; Bigliardi, G. *Acta Crystallogr.* **1963**, *16*, 846.
(48) Gregory, N. W.; Wydeven, T. *J. Phys. Chem.* **1963**, *67*, 927.
(49) Wyckoff, R. W. G. *Crystal Structures*, 2 ed.; Robert E. Krieger Publishing Co.: Malabar, FL, 1982; Vol. 1, pp 268, 416.
(50) Beattie, J. K.; Moore, C. J. *Inorg. Chem.* **1982**, *21*, 1292.
(51) Hamilton, W. C. *Acta Crystallogr.* **1962**, *15*, 353.
(52) Price, D. C. *Can. J. Phys.* **1987**, *65*, 1280.
(53) Montgomery, H.; Chastain, R. V.; Natt, J. J.; Witkowska, A. M.; Lingafelter, E. C. *Acta Crystallogr.* **1967**, *22*, 775.
(54) Burbridge, C. D.; Goodgame, D. M. L. *Inorg. Chim. Acta* **1970**, *4*, 231.
(55) Miller, L. L.; Jacobsen, R. A.; Chen, Y.-S.; Kurtz, D. M., Jr. *Acta Crystallogr.* **1989**, *C45*, 527.
(56) Lauher, J. W.; Ibers, J. A. *Inorg. Chem.* **1975**, *14*, 348.
(57) Briat, B.; Canit, J. C. *Mol. Phys.* **1983**, *48*, 33.
(58) Kitajima, N. Private communication, 1994.
(59) Pabst, A. *Am. Minerol.* **1943**, *28*, 372.
(60) Pabst, A. *Acta Crystallogr.* **1959**, *12*, 733.

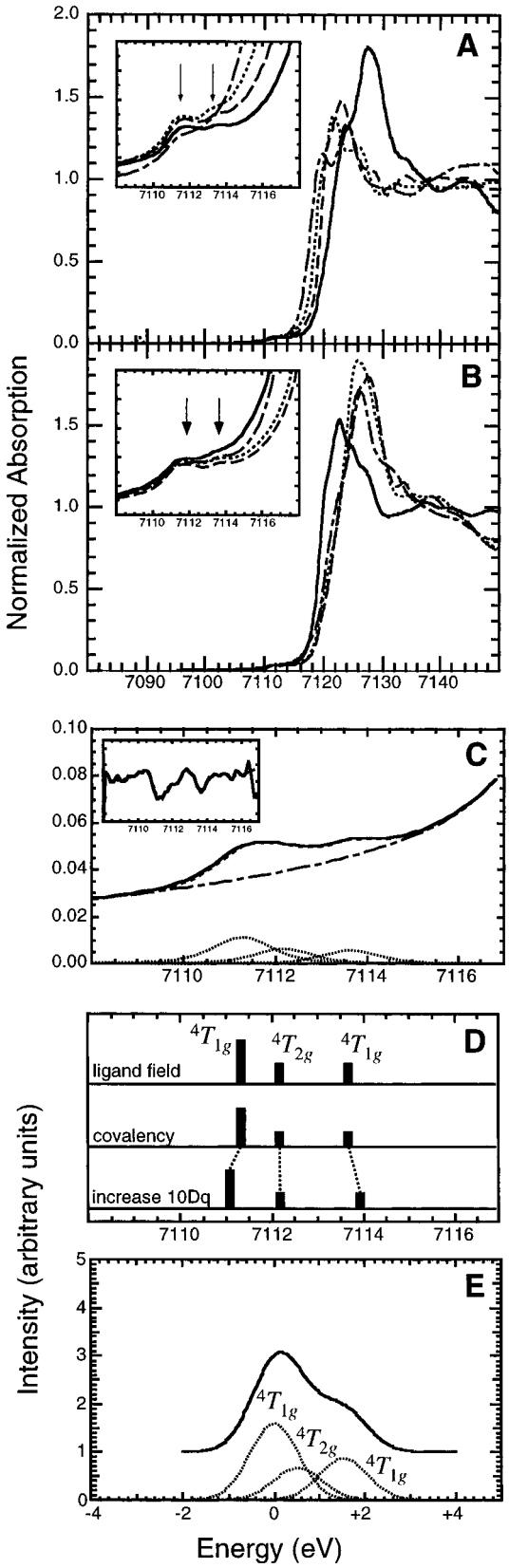

Figure 1. Fe K-edge XAS spectra, pre-edge fits, and theoretical analysis and simulation of octahedral high-spin Fe^{II} complexes. Fe K-edge spectra of (A) FeF_2 (—), $FeCl_2$ (- - -), $FeBr_2$ (···), and FeI_2 (— -) and (B) rinneite (—), $[Fe(H_2O)_6][SiF_6]$ (- - -), $[Fe(H_2O)_6](NH_4)_2(SO_4)_2$ (···), and $[Fe(imidazole)_6]Cl_2$ (— -). The insets show expanded views of the 1s → 3d pre-edge region with the normalized absorption scale set from 0 to 0.1 in each case. (C) The Fe K-edge pre-edge region of $[Fe(H_2O)_6][SiF_6]$ including the experimental data (—), a fit to the data (- - -), the background function (— -), and the individual pre-edge peaks from the fit (···). The inset displays the second derivative of the data (—) and the second derivative of the fit (- - -). (D) Ligand field analysis of $[Fe(H_2O)_6][SiF_6]$ (see text) including the energy splittings determined by ligand field theory, the effect of covalency differences in the final states, and the predicted effect of increasing 10*Dq* of the octahedral complex. (E) Theoretical simulation of the pre-edge region for $[FeCl_6]^{4-}$ based on single-determinant density functional calculations of the $^4T_{1g}$, $^4T_{2g}$, and $^4T_{1g}$ final states. Gaussian band shapes were used to simulate each XAS pre-edge transition with a FWHM peak width of 0.75 eV. Energy splittings are shown relative to the energy of the lowest-energy final state, and covalency differences for each state are calculated from 3d contributions to acceptor orbitals in the final states.

Scheme 1

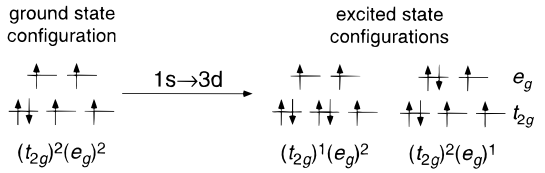

by ∼2 eV as indicated by arrows in the insets. A fit to the pre-edge region of $[Fe(H_2O)_6][SiF_6]$ is shown in Figure 1C and is representative of the fit qualities obtained. Two peaks were required to fit the first feature at ∼7111.5 eV as there is clearly a shoulder in the second derivative of the data at ∼7112 eV (Figure 1C inset).

The 1s → 3d transition is formally electric dipole forbidden, but gains intensity through the allowed electric quadrupole transition. Since all eight of these complexes have a nearly centrosymmetric octahedral iron site, electric dipole intensity cannot be gained by mixing of the *gerade* 3d orbitals with the *ungerade* 4p orbitals. The splitting of the high-spin ferrous pre-edge feature has previously been attributed to the $d^{(n+1)}$ free ion splitting of the ^4F and ^4P terms.[20] However, the octahedral ligand field around the iron causes splitting of the 3d orbitals into a t_{2g} and an e_g set. Removing the degeneracy of the 3d orbitals causes the ^4F and ^4P terms to split into four many-electron states ($^4T_{1g}$, $^4T_{2g}$, $^4T_{1g}$, and $^4A_{2g}$)[90] and should significantly impact the assignment of XAS pre-edge features.

The $^5T_{2g}$ ground state of a high-spin ferrous atom in an O_h ligand field has an electronic hole configuration of $(t_{2g})^2(e_g)^2$. Promotion of an electron from a 1s orbital into the 3d manifold gives the excited hole configurations shown in Scheme 1. Coupling of the valence holes in these configurations gives the parent $d^{(n+1)}$ strong-field many-electron excited states.[90] The $(t_{2g})(e_g)^2$ configuration gives rise to a $^4T_{1g}$ state while the $(t_{2g})^2(e_g)$ configuration gives a $^4T_{1g}$ and a $^4T_{2g}$ state. The $^4A_{2g}$ state originates from a two-electron excited $(t_{2g})^3$ hole configuration and thus will not contribute to the pre-edge region; it also cannot mix with any of the one-electron allowed states from symmetry considerations. The complete final states must include the hole in the 1s orbital created by promotion of the electron to the valence 3d manifold. The 1s hole is totally symmetric (a_{1g}); it will not affect the symmetry of the final states. Spin coupling with the parent excited states, however, yields a set of one-electron quintet ($^5T_{1g}$, $^5T_{2g}$, $^5T_{1g}$) and triplet ($^3T_{1g}$, $^3T_{2g}$, $^3T_{1g}$) states. For the $^5T_{2g}$ ground state, only the quintet final states correspond to spin-allowed transitions. These states will have the same relative energy splittings as the parent $d^{(n+1)}$ excited states. The parent state labels will be used throughout for direct correspondence with the Tanabe−Sugano matrices in the ligand field analysis.

The energies of the $^4T_{1g}$, $^4T_{2g}$, and $^4T_{1g}$ states can be determined by solving the $d^{(n+1)}$ Tanabe−Sugano matrices[92] with appropriate values for the ligand field parameters (10*Dq*, *B*, and *C*). Ground state 10*Dq* values may be obtained from optical spectroscopy, but XAS excited state 10*Dq* values should be reduced because of the additional electron in the Fe 3d manifold. It has been found that 10*Dq* values obtained from charge transfer

Table 1. XAS Pre-Edge Energies and Intensities for High-Spin Iron Model Complexes

compound	oxidation state	symm	ligation	beamline, temperature	pre-edge peak energy[a]	pre-edge peak int[a,b]	total pre-edge peak int[b]	peak energy difference[c]	peak int ratio[d]	ref
FeF_2	ferrous	O_h	6 F	SSRL 7-3,10 K	7111.38(0.03)	2.2(0.2)	4.4(0.2)	2.1	0.73	46
					7112.28(0.09)	1.0(0.1)				
					7113.48(0.06)	1.2(0.2)				
$FeCl_2$	ferrous	O_h	6 Cl	SSRL 7-3,10 K	7111.32(0.05)	1.9(0.4)	4.3(0.2)	2.1	0.78	47
					7112.05(0.11)	1.4(0.6)				
					7113.42(0.05)	0.9(0.2)				
$FeBr_2$	ferrous	O_h	6 Br	SSRL 7-3,10 K	7111.32(0.03)	2.5(0.6)	3.8(0.3)	1.8	0.84	48
					7111.98(0.25)	0.7(0.8)				
					7113.15(0.04)	0.6(0.1)				
FeI_2	ferrous	O_h	6 I	SSRL 4-3,30 K	7111.35(0.05)	2.2(0.2)	3.1(0.2)	1.3	0.73	49
					7112.70(0.10)	0.8(0.2)				
rinneite ($K_3NaFeCl_6$)	ferrous	O_h	6 Cl	SSRL 7-3,10 K	7111.32(0.06)	1.2(0.9)	3.6(0.2)	2.1	0.84	50
					7111.81(0.19)	1.8(1.2)				
					7113.38(0.04)	0.6(0.1)				
$[Fe(H_2O)_6][SiF_6]$	ferrous	O_h	6 O	SSRL 2-3,10 K	7111.34(0.07)	2.2(0.5)	4.0(0.5)	2.3	0.73	51, 52
					7112.26(0.08)	0.7(0.3)				
					7113.60(0.04)	1.1(0.3)				
$[Fe(H_2O)_6](NH_4)_2(SO_4)_2$	ferrous	O_h	6 O	SSRL 2-3,10 K	7111.18(0.07)	1.5(0.6)	3.9(0.3)	2.4	0.77	53
					7112.03(0.15)	1.6(0.7)				
					7113.58(0.03)	0.9(0.2)				
$[Fe(imidazole)_6]Cl_2$	ferrous	O_h	6 N	SSRL 2-3,10 K	7111.24(0.03)	1.6(0.5)	3.8(0.3)	2.4	0.85	54, 55
					7112.35(0.16)	1.6(0.8)				
					7113.66(0.02)	0.6(0.2)				
$(Et_4N)_2[FeCl_4]$	ferrous	T_d	4 Cl	SSRL 7-3,10 K	7111.60(0.02)	8.6(0.4)	12.9(0.6)	1.5	0.67	56
					7113.12(0.02)	4.3(0.7)				
Cs_3FeCl_5	ferrous	T_d (D_{2d})	4 Cl	SSRL 2-3,10 K	7111.60(0.01)	9.8(0.3)	13.1(0.4)	1.5	0.75	57
					7113.11(0.01)	3.3(0.3)				
Fe(HB(3,5-*i*Pr_2pz)$_3$)Cl	ferrous	T_d (C_{3v})	3 N, 1 Cl	SSRL 2-3,10 K	7111.64(0.02)	14.2(0.5)	19.8(0.9)	1.5	0.72	58
					7113.17(0.02)	5.6(0.9)				
gillespite ($BaFeSi_4O_{10}$)	ferrous	D_{4h}	4 O	SSRL 4-3,100 K	7111.74(0.02)	4.1(0.3)	5.3(0.3)	1.5	0.78	59, 60
					7113.25(0.03)	1.2(0.2)				
$[Fe(TMC)Cl](BF_4)$	ferrous	C_{4v}	4 N, 1 Cl	SSRL 7-3,300 K	7111.41(0.01)	10.9(0.1)	12.9(0.2)	2.0	0.84	61
					7113.43(0.02)	2.0(0.3)				
$[Fe(TMC)Br](BF_4)$	ferrous	C_{4v}	4 N, 1 Br	SSRL 7-3,300 K	7111.35(0.01)	9.0(0.3)	11.1(0.3)	1.9	0.81	61
					7113.24(0.04)	2.1(0.4)				
$[Fe(TMC)CH_3CN](BF_4)_2$	ferrous	C_{4v}	4 N, 1 N (CH_3CN)	SSRL 7-3,300 K	7111.52(0.04)	10.5(0.8)	12.7(0.5)	1.8	0.83	61
					7113.30(0.12)	2.2(1.2)				
$[Fe(TMC)N_3](BF_4)$	ferrous	C_{4v}	4 N, 1 N (N_3)	SSRL 7-3,300 K	7111.47(0.01)	12.4(0.5)	13.4(0.3)	1.8	0.92	61
					7113.30(0.05)	1.0(0.2)				
FeF_3	ferric	O_h	6 F	SSRL 4-3,55 K	7113.38(0.02)	3.3(0.2)	5.3(0.3)	1.4	0.63	62
					7114.79(0.02)	1.9(0.2)				
$FeCl_3$	ferric	O_h	6 Cl	SSRL 4-3,30 K	7112.60(0.02)	2.2(0.2)	4.0(0.2)	1.2	0.54	63
					7113.77(0.03)	1.8(0.2)				
$FeBr_3$	ferric	O_h	6 Br	SSRL 4-3,30 K	7112.37(0.02)	2.6(0.2)	4.4(0.2)	1.1	0.59	63
					7113.52(0.03)	1.8(0.2)				
$[FeCl_6][Co(NH_3)_6]$	ferric	O_h	6 Cl	SSRL 7-3,10 K	7112.78(0.03)	2.6(0.3)	4.0(0.2)	1.2	0.65	50, 64
					7114.02(0.03)	1.4(0.1)				
$Fe(acac)_3$	ferric	O_h	6 O	SSRL 4-3,55 K	7112.79(0.02)	2.7(0.3)	4.6(0.3)	1.5	0.59	65
					7114.31(0.04)	1.9(0.1)				
$[Fe(urea)_6](ClO_4)_3$	ferric	O_h	6 N	SSRL 7-3,10 K	7112.97(0.02)	2.6(0.2)	4.5(0.3)	1.5	0.58	66
					7114.44(0.02)	1.9(0.1)				
$(NH_4)_3[Fe(malonate)_3]$	ferric	O_h	6 O	SSRL 2-3,10 K	7112.92(0.03)	3.1(0.3)	5.5(0.1)	1.5	0.57	67
					7114.44(0.03)	2.4(0.3)				
$K_3[Fe(oxalate)_3]\cdot 2H_2O$	ferric	O_h	6 O	SSRL 2-3,10 K	7112.93(0.00)	4.9(0.1)	7.3(0.2)	1.5	0.67	68
					7114.41(0.01)	2.4(0.1)				
$[Fe(H_2O)_6](NH_4)(SO_4)_2\cdot 6H_2O$	ferric	O_h	6 O	SSRL 2-3,10 K	7113.14(0.02)	2.7(0.1)	4.9(0.2)	1.4	0.56	69
					7114.57(0.01)	2.2(0.2)				
$(Et_4N)[FeCl_4]$	ferric	T_d	4 Cl	SSRL 7-3, 10 K	7113.16(0.00)	20.7(0.8)	20.7(0.8)			70
Fe(salen)Cl	ferric	C_{4v}	2 O, 2 N, 1 Cl	SSRL 7-3,10 K	7112.91(0.01)	12.9(0.3)	14.4(0.6)	1.3	0.89	71
					7114.25(0.07)	1.5(0.4)				

[a] Pre-edge energies and intensities were determined by fits to the data (see the Experimental Section for details on the fitting procedure). [b] The values reported for the pre-edge intensities were multiplied by 100. [c] Peak energy differences are the energy differences between the lowest energy and the highest energy pre-edge features. [d] Peak intensity ratios are the intensity of the first pre-edge feature divided by the total pre-edge intensity. In the case of most ferrous octahedral complexes, which required three peaks to fit the pre-edge feature, the peak intensity ratios are the intensity of the first two peaks required to fit the first feature divided by the total pre-edge intensity (all discrepencies are attributable to roundoff in the reporting of peak intensities).

transition energies are ~63% of the values obtained from ligand field transitions.[93] For XAS transitions, the excited state 10*Dq* should not be as reduced due to the increased effective nuclear charge from the 1s hole. The energies of the many-electron states were calculated with a 10*Dq* that is 80% of the ground state value (*vide infra*). The *B* value used was a $d^{(n+1)}$ free ion *B* value reduced by 10% ($\beta = 0.9$) to include covalency effects.

(61) Hodges, K. D.; Wollmann, R. G.; Barefield, E. K.; Hendrickson, D. N. *Inorg. Chem.* **1977**, *16*, 2746.
(62) Hepworth, M. A.; Jack, K. H.; Peacock, R. D.; Westland, G. J. *Acta Crystallogr.* **1957**, *10*, 63.
(63) Gregory, N. W. *J. Am. Chem. Soc.* **1951**, *73*, 472.
(64) Hatfield, W. E.; Fay, R. C.; Pfluger, C. E.; Piper, T. S. *J. Am. Chem. Soc.* **1963**, *85*, 265.
(65) Iball, J.; Morgan, C. H. *Acta Crystallogr.* **1967**, *23*, 239.
(66) Holt, S.; Dingle, R. *Acta Chem. Scand.* **1968**, *22*, 1091.

The *C*/*B* ratio was kept fixed at 4.0. High-spin ferrous complexes such as $[Fe(H_2O)_6]^{2+}$ typically have ground state $10Dq$ values of ~10 000 cm^{-1}.[94] Using $10Dq = 8000$ cm^{-1}, $B = 780$ cm^{-1}, and $C = 3120$ cm^{-1}, the energies of the $^4T_{1g}$, $^4T_{2g}$, and $^4T_{1g}$ states were determined from the d^7 Tanabe−Sugano matrices. The lowest energy excited state is the $^4T_{1g}$ state ($0.08|(t_{2g})^2(e_g)\rangle + 0.92|(t_{2g})(e_g)^2\rangle$). The $^4T_{2g}$ ($|(t_{2g})^2(e_g)\rangle$) and $^4T_{1g}$ ($0.92|(t_{2g})^2(e_g)\rangle + 0.08|(t_{2g})(e_g)^2\rangle$) states are 0.9 and 2.2 eV above the lowest state, respectively. The ligand field analysis, therefore, predicts three pre-edge features split by 0.9 and 1.3 eV for $[Fe(H_2O)_6]^{2+}$ (see Figure 1D, ligand field). The first two features would be barely resolvable as the energy resolution at the Fe K-edge is ~1.4 eV.[32] These energy splittings are consistent with the experimental data for $[Fe(H_2O)_6][SiF_6]$. The relative intensities of the transitions should depend on the statistically weighted number of one-electron XAS transition pathways from the ground state to the final state; the intensity of the $(t_{2g})(e_g)^2$-derived $^4T_{1g}$ final state should be equal to the combined intensities of the $(t_{2g})^2(e_g)$-derived final states ($^4T_{1g}$ and $^4T_{2g}$). The ratio of intensities is thus predicted to be $(0.92 \times 6/3 + 0.08 \times 3/3):(3/3):(0.08 \times 6/3 + 0.92 \times 3/3)$ or 1.92:1.00:1.08.[95] The intensities of these three features will also be perturbed due to covalent mixing of the 3d orbitals with the ligand valence orbitals. Covalent interactions with the ligands will decrease the Fe 3d character in the final states and thus decrease the intensity of the electric quadrupole transition. The e_g set of 3d orbitals is more covalent than the t_{2g} set due to its σ rather than π bonding interactions with the ligands. Transitions to states containing a $(t_{2g})(e_g)^2$ component should be more intense than states containing a $(t_{2g})^2(e_g)$ component as there is more Fe 3d (electric quadrupole-allowed) character in the t_{2g} set of orbitals. In the high-spin ferrous case, only the lowest energy $^4T_{1g}$ state contains a significant $(t_{2g})(e_g)^2$ component. Covalency will cause a decrease in the electric quadrupole intensity relative to that predicted for transitions to atomic 3d orbitals, with the lowest energy feature decreasing to a lesser extent than the two features at higher energy (see Figure 1D, covalency). All of the ferrous high-spin octahedral model complex pre-edge features required a three-peak fit (with the exception of FeI_2 which was adequately fit with two features), with the lower energy feature being more intense than the other two features (see Table 1 and Figure 1). These experimental data are thus consistent with the analysis above.

DFT final state calculations on $[FeCl_6]^{4-}$ predict the same energy pattern as the ligand field analysis for $[Fe(H_2O)_6]^{2+}$ with smaller energy splittings between the three final states, which is consistent with the weaker field provided by the chloride ligands. However, the splitting between the two $^4T_{1g}$ $d^{(n+1)}$ states is calculated to be 1.6 eV for the ferrous chloride complex. Ligand field analysis for the chloride complex predicts a somewhat larger splitting (~1.8 eV) than the density functional approach. The lower splitting is not surprising due to the fact that the density functional calculations are single-determinant solutions and do not directly account for configurational interaction (CI) between the two $^4T_{1g}$ final states. CI can be estimated from the solutions to the Tanabe−Sugano matrices (*vide supra*); in this case, CI causes nearly 10% mixing of the two $^4T_{1g}$ states. The molecular orbital calculations also indicate that the e_g acceptor orbitals (~75% 3d character) are significantly more covalent than the t_{2g} orbitals (~90% 3d character), in accordance with expected behavior (*vide supra*). A simulated pre-edge spectrum can be constructed from the results of the final state DFT calculations (see Figure 1E) assuming a linear relationship between the intensity of a transition and the Mulliken population statistics obtained from the calculation. This spectrum differs from the ligand field theory-derived prediction (Figure 1D) and the experimental data (Figure 1C) only in the magnitude of the $^4T_{1g}$ splitting.

The total normalized pre-edge intensities of the octahedral high-spin ferrous complexes range from 3.1 to 4.4 with an average intensity of 3.9 normalized units (see Table 1) and reflects a pure electric quadrupolar contribution to the transition. Experimental trends in the pre-edge splittings of the three features in these complexes can be related to ligand field strength: $Fe^{II}(imidazole)_6 > Fe^{II}(H_2O)_6 > FeF_2 \approx FeCl_2 > FeBr_2 > FeI_2$. This is the same trend that is observed for $10Dq$ values obtained from optical spectroscopy along the spectrochemical series.[94] The final state energies are dominated by the multiplet splitting effects, resulting in only relatively small changes in the splitting upon changing the ligand field. Increasing the ligand field strength will increase the splitting between the low-energy $^4T_1$ and $^4T_2$ states and the two $^4T_1$ states, but the energy splitting between the $^4T_2$ and the higher energy $^4T_1$ state reflects predominantly the multiplet splitting of the final states (see Figure 1D, increase $10Dq$).

B. T_d Geometry. Fe K-edge XAS data were measured for three ferrous tetrahedral complexes: $(Et_4N)_2[FeCl_4]$, Cs_3FeCl_5, and Fe(HB(3,5-*i*Pr$_2$pz)$_3$)Cl. The iron environment in $(Et_4N)_2[FeCl_4]$ is very near T_d symmetry, while Cs_3FeCl_5 and Fe(HB(3,5-*i*Pr$_2$pz)$_3$)Cl are D_{2d} and C_{3v} distorted, respectively. The XAS edge spectra for these three complexes are shown in Figure 2A with an expanded view of the 1s → 3d pre-edge region presented in the inset. All three complexes have a relatively intense pre-edge feature that is split by 1.5 eV, with the lower energy feature being more intense than the higher energy feature (see Table 1, Figure 1B). The Fe(HB(3,5-*i*Pr$_2$pz)$_3$)Cl pre-edge peaks are more intense than those of $(Et_4N)_2[FeCl_4]$ and Cs_3FeCl_5. A fit to the pre-edge region of $(Et_4N)_2[FeCl_4]$ is shown in Figure 2B.

The 1s → 3d pre-edge features of all three complexes can gain intensity through both electric quadrupole and electric dipole intensity mechanisms. The electric dipole mechanism involves 4p mixing into the 3d orbitals in a noncentrosymmetric environment around the iron site. In T_d symmetry, the ^5E ground state has a $(t_2)^3(e)^1$ hole configuration, and therefore, the only one-electron allowed excited states are those shown in Scheme 2. Final states involving a $(t_2)^1(e)^2$ configuration would involve a forbidden two-electron transition.

Electron coupling in the $(t_2)^3(e)^0$ hole configuration gives a $^4A_2$ many-electron state, while coupling in the $(t_2)^2(e)^1$ hole configuration gives $^4T_1$ and $^4T_2$ states. The two-electron $(t_2)^1(e)^2$ configuration also gives rise to a $^4T_1$ state. Since the two $^4T_1$ states are allowed to mix by symmetry, both $^4T_1$ states will have a one-electron allowed $(t_2)^2(e)^1$ component. The $^4A_2$ and the $^4T_2$ states contain only $(t_2)^3(e)^0$ and $(t_2)^2(e)^1$ components, respectively, and transitions into these states are fully allowed.

Energies of the four many-electron states were estimated from Tanabe−Sugano matrices using a $10Dq$ value of 3280 cm^{-1} (80% of the ground state $10Dq$ of $(Et_4N)_2[FeCl_4]$),[96] a *B* value of 780 cm^{-1} (90% of the $d^{(n+1)}$ B), and a *C* value of 3120 cm^{-1}. The $^4A_2$ ($|(t_2)^3(e)^0\rangle$) state is the lowest energy excited state (set at 0.0 eV relative energy) followed by the $^4T_2$ ($|(t_2)^2(e)^1\rangle$) state at 0.4 eV, the lower energy $^4T_1$ state ($0.31|(t_2)^2(e)^1\rangle + 0.69|(t_2)^1(e)^2\rangle$) at 0.7 eV, and the higher energy $^4T_1$ state ($0.69|(t_2)^2(e)^1\rangle + 0.31|(t_2)^1(e)^2\rangle$) is at 2.0 eV. Since the $(t_2)^1(e)^2$ configuration requires a two-electron transition, only the $(t_2)^2(e)^1$ components of the $^4T_1$ states will contribute transition intensity. The three lower energy states ($^4A_2$, $^4T_2$, and $^4T_1$) are

(67) Jaeger, F. M.; Mees, R. T. A. *Proc. Acad. Sci. Amsterdam* **1918**, *20*, 283.
(68) Clark, H. C.; Curtis, N. F.; Odell, A. L. *J. Chem. Soc.* **1954**, 63.
(69) Wyckoff, R. W. G. *Crystal Structures*, 2nd ed.; Robert E. Krieger Publishing Co.: Malabar, FL, 1982; Vol. 3, pp 875, 898.
(70) Kistenmacher, T. J.; Stucky, G. D. *Inorg. Chem.* **1968**, *7*, 2150.
(71) Gerloch, M.; Mabbs, F. E. *J. Chem. Soc.* **1967**, 1598.

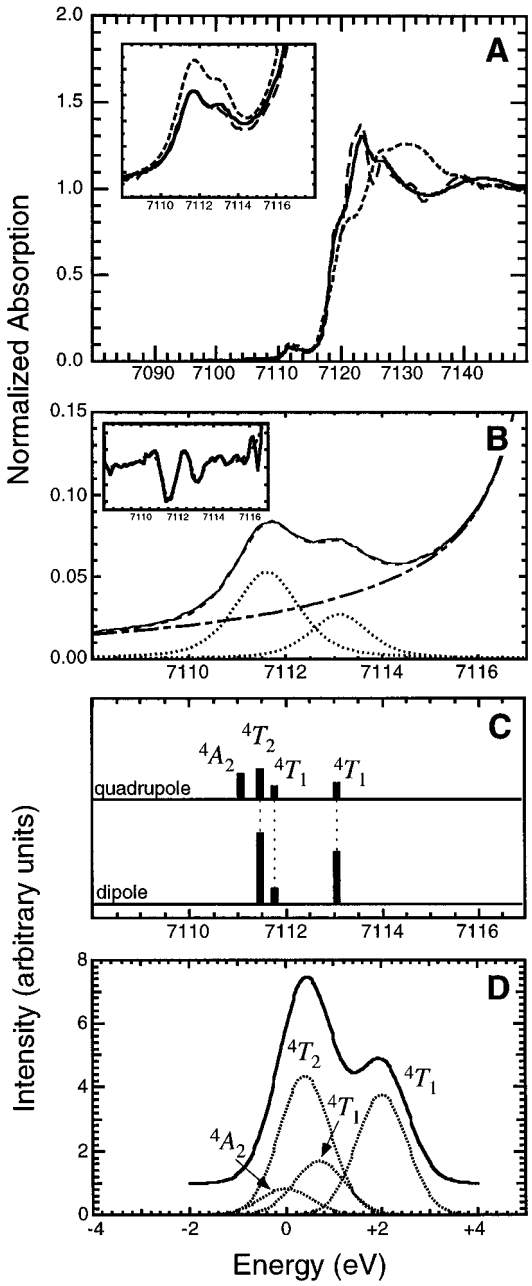

Figure 2. Fe K-edge XAS spectra, pre-edge fits, and theoretical analysis and simulation of tetrahedral high-spin Fe^{II} complexes. (A) Fe K-edge spectra of $(Et_4N)_2[FeCl_4]$ (—), Cs_3FeCl_5 (- - -), and Fe(HB(3,5-*i*Pr_2pz)$_3$)Cl (···) with an expanded view of the 1s → 3d pre-edge region in the inset; the normalized absorption scale is 0.00−0.12. (B) Fit to the Fe K-edge pre-edge region of $(Et_4N)_2[FeCl_4]$ including the experimental data (—), a fit to the data (- - -), the background function (— -), and the individual pre-edge peaks from the fit (···). The inset displays the second derivative of the data (—) and the second derivative of the fit to the data (- - -). (C) Theoretical energy splitting and intensity distribution in the $^4A_2$, $^4T_2$, $^4T_1$, and $^4T_1$ final states through both the electric quadrupole and electric dipole intensity mechanisms. (D) Theoretical simulation of the pre-edge region for $[FeCl_4]^{2-}$ based upon density functional calculations and configuratonal interaction (see text) for the $^4A_2$, $^4T_2$, $^4T_1$, and $^4T_1$ final states. The full simulated spectrum is shown as a solid line, with all component features shown as dotted lines.

all within 0.7 eV of each other and should not be resolvable at the Fe K-edge, while the higher energy $^4T_1$ state is positioned 2 eV higher than the $^4A_2$ state and should be resolvable.

The electric quadrupole intensity is divided among these final states according to the degeneracy of the state, the weighted number of transition pathways, and the percentage of the one-electron allowed strong field component (in the case of the $^4T_1$ states). The electric quadrupole intensity ratio of the $^4A_2$:$^4T_2$:$^4T_1$:$^4T_1$ is (1 × 2/2):(3/2):(0.31 × 3/2):(0.69 × 3/2) or 1.00:1.50:0.46:1.04 (see Figure 2C, quadrupole). The pre-edge features of these tetrahedral complexes will also gain intensity from 4p mixing into the 3d orbitals. The 4p orbitals transform as t_2 so they will only mix with the 3d t_2 orbitals and, thus, only the $d^{(n+1)}$ states that have a $(t_2)^2(e)^1$ component (see Scheme 2) will gain electric dipole intensity. The $^4T_2$, $^4T_1$, and $^4T_1$ states have a $(t_2)^2(e)^1$ component and will have a relative electric dipole intensity ratio of (3/2):(0.31 × 3/2):(0.69 × 3/2) or 1.50:0.46:1.04, respectively (Figure 2D, dipole). Consequently, two pre-edge features are expected, with the first feature containing transitions into the $^4A_2$,$^4T_2$, and $^4T_1$ states and the second feature containing the transition into the higher energy $^4T_1$ state.

Scheme 2

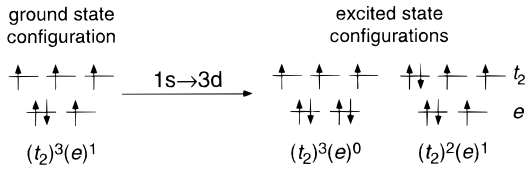

DFT calculations can also be used to evaluate the distribution of 4p character over the Fe 3d orbitals, generate a reasonable prediction of the pre-edge spectrum, and estimate the overall amount of 4p mixing in the final states. The one drawback to the single-determinant density functional calculation is the inability to properly evaluate strong CI between the final states of $^4T_1$ symmetry. Ground state calculations for $FeCl_4^{2-}$ indicate a strong 4p contribution to the t_2 valence orbitals (1.8% 4p in each orbital). Final state calculations also indicate significant 4p mixing into the t_2 set of orbitals which distribute within the $^4T_2$ and two $^4T_1$ final states. The total amount of 4p mixing in the Fe 3d acceptor orbitals is calculated as 5.4% in the ground state. Only with the inclusion of 4p mixing, can the experimental intensity be explained adequately. A simulated pre-edge spectrum is shown in Figure 2D using relative energies and configurational interaction parameters as calculated from Tanabe−Sugano matrices and orbital contributions from the density functional calculations. The intensity distribution between the two observable features is very similar to the experimental distribution; the ratio of the low-energy feature to the total intensity is calculated to be 0.66, and the experimental ratio is 0.67. An important conclusion from the DFT calculations is that 4p character distributes into the t_2 orbitals and thus distributes electric dipole character into the three high-energy one-electron allowed final states.

Using an estimated total electric quadrupole intensity of 3.9-(0.5) as determined from the ferrous octahedral intensities, the experimental electric dipole intensity of $(Et_4N)_2[FeCl_4]$ is 9.0-(0.6) (see Table 1). The percentage of 4p mixing into the 3d orbitals can be estimated from this experimental electric dipole intensity. The intensity of electric quadrupole-allowed transitions should be ∼1% of electric dipole-allowed transitions as calculated by Blair and Goddard[24] and experimentally observed for $CuCl_4^{2-}$.[97,98] A more rigorous relationship can be obtained from comparative analysis of the pre-edge features of $(creatininium)_2CuCl_4$, a D_{4h} complex, and Cs_2CuCl_4, a D_{2d} complex. The fitted 1s → 3d pre-edge intensities of these two complexes are 1.5(0.3) and 7.1(0.5), respectively. The pre-edge feature of the centrosymmetric $(creatininium)_2CuCl_4$ complex has only electric quadrupole intensity from a transition into $3d_{x^2-y^2}$, while the pre-edge feature of Cs_2CuCl_4 has both electric quadrupole intensity from a transition into $3d_{x^2-y^2}$ and electric dipole intensity from $4p_z$ mixing into the $3d_{x^2-y^2}$ acceptor orbital. The electric quadrupole contributions to the pre-edge for both

complexes should be similar, once corrected for covalency differences. Taking into account the differences in 3d character in the lowest unoccupied molecular orbital (61% for $(creatininium)_2CuCl_4$ and 67% for Cs_2CuCl_4[97,98]), the amount of electric quadrupole intensity in the pre-edge feature of Cs_2CuCl_4 should be 1.65(0.4). The amount of electric dipole intensity in the pre-edge feature of Cs_2CuCl_4 should therefore be 7.1(0.5) − 1.65(0.4) = 5.45(0.6). Analysis of the Cu 1s → 4p + LMCT shakedown transition has experimentally determined that the acceptor orbital contains 3.8(1.5)% $4p_z$ character.[97,98] This means that 1.4(0.6) units of intensity correspond to 1% 4p mixing in Cu(II) complexes. This relationship between the intensity of the electric dipole contribution to a pre-edge feature and the amount of 4p character in the final state can be extended to Fe(II) complexes by correcting for normalization and 1s → 4p transition probabilities. The normalization procedure sets the post-edge continuum region to unity, and thus, a correction must be applied based on photoionization cross section differences for the 1s electron of Cu(II) and Fe(II);[99] the intensity for the Fe(II) 1s → continuum is ∼128% that of Cu(II).[100] The 1s → 4p transition probabilities are directly related to their oscillator strengths (f_{4p}), which depend on the effective nuclear charge felt by the excited electron in both the initial and final states. Equation 1 was

$$f_{4p} \propto \left[\frac{(Z_{1s})^{3/2}(Z_{4p})^{5/2}(5(Z_{4p})^2 - 2(Z_{1s})(Z_{4p}) - 12(Z_{1s})^2)}{((Z_{4p}) + 2(Z_{1s}))^7}\right]^2 \quad (1)$$

derived[101] from evaluation of the transition moment integral squared for an electric dipole-coupled 1s → 4p transition using hydrogenic wave functions. The relative oscillator strengths for Cu(II) and Fe(II) were determined using simple estimates of Z_{1s} and Z_{4p}. Since the transition occurs into a molecular orbital with predominantly Fe 3d character, the effective nuclear charges in the final states are estimated by values for Fe 3d atomic orbitals, Z_{3d}.[102,103] The Fe(II) oscillator strength is calculated to be 68% of that for Cu(II). The relationship between intensity and 4p mixing is therefore 1.22(0.5) units for 1% Fe(II) 4p character.

With this information, the amount of 4p mixing into the 3d orbitals for $(Et_4N)_2[FeCl_4]$ is calculated to be 7.4(3.0)%. Note that the most significant error in the estimate of 4p character is derived from the inherent error in the quantitation of 4p character in the final state of the Cs_2CuCl_4 reference complex (*vide infra*). This error propagates through all estimates of 4p character from experimental intensities; it does not reflect the error in the experimental intensities and should not affect trends determined on the basis of these experimental intensities. The theoretically calculated 4p mixing (5.4%) and predicted pre-edge spectrum is in reasonable agreement with experiment.

C. C_{4v} Geometry. Fe K-edge XAS data were measured for four square pyramidal high-spin ferrous model complexes: [Fe(TMC)Cl](BF_4), [Fe(TMC)Br](BF_4), [Fe(TMC)CH_3CN](BF_4)$_2$, and [Fe(TMC)N_3](BF_4). The spectra of these four complexes are shown in Figure 3A with an expanded view of the 1s → 3d pre-edge region shown in the inset. All four of these square pyramidal complexes have an intense feature at ∼7111.5 eV, with a second much weaker feature indicated by the arrow at ∼7113.3 eV which, however, is clearly visible from the second derivative (Figure 3B, inset). [Fe(TMC)N_3](BF_4) has the most intense pre-edge feature while that of [Fe(TMC)Br](BF_4) is the least intense (Table 1). A fit to the pre-edge region of [Fe(TMC)Cl](BF_4) is shown in Figure 3B.

An iron atom in a C_{4v} site is in a noncentrosymmetric environment, and thus the 1s → 3d pre-edge transition may gain intensity from both the allowed electric quadrupole and 3d−4p mixing (electric dipole) mechanisms. A C_{4v} site can be initially treated (*vide supra*) as a distorted O_h site in which the $^4T_2$ $d^{(n+1)}$ state splits into a $^4B_2$ and a ^4E state and the two $^4T_1$ states split into $^4A_2$ and ^4E states. If the ground state orbital splitting is as shown in Scheme 3 (the $^5T_2$ splits into a $^5B_2$ and a ^5E, the $^5B_2$ being lowest in these systems), then promotion of a 1s electron into the 3d manifold produces three $d^{(n+1)}$ allowed one-electron excited state (hole) configurations: $(e)^1(a_1)^1(b_1)^1$, $(e)^2(a_1)^0(b_1)^1$, and $(e)^2(a_1)^1(b_1)^0$ (Scheme 3).

Scheme 3

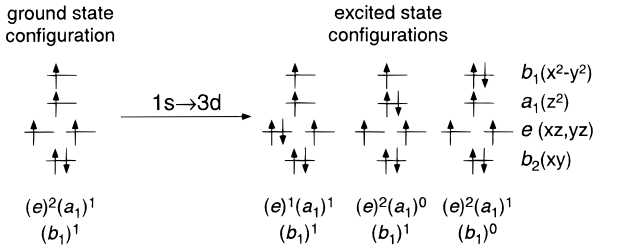

The relative energies of the one-electron configurations were determined from DFT calculations on the Fe(TMC)X model systems (X = Cl, Br). The results are consistent with values obtained from optical absorption experiments for square pyramidal ferrous complexes.[94] From these calculations, the $(e)^2(a_1)^0(b_1)^1$ configuration (which contributes to the $^4B_2$ state from the O_h $^4T_2$ state) is actually lowest in energy, with the $(e)^1(a_1)^1(b_1)^1$ configuration (^4E from the lower energy O_h $^4T_1$ state) being 0.4 eV higher in energy, and the $(e)^2(a_1)^0(b_1)^1$ configuration ($^4A_2$ from the higher energy O_h $^4T_1$ state) being 1.6 eV above that. The many-electron $^4B_2$, ^4E, and $^4A_2$ final states should all contain electric quadrupole intensity. Neglecting differences in covalency, the electric quadrupole contribution to these final states should have an intensity ratio of 1:2:1, respectively (see Figure 3C). It is noteworthy that low-energy two-electron excited ^4E and $^4A_2$ final states can configurationally interact with the appropriate allowed final states, redistributing the electric quadrupole intensity and changing the energy positions of these transitions. However, the $^4B_2$ state will remain unaffected by configurational interaction.

The pre-edge features of these square pyramidal complexes can further gain intensity from 4p mixing into the 3d orbitals. In C_{4v}, the 4p orbitals transform as e ($4p_{x,y}$) and a_1 ($4p_z$). As the main distortion is along the *z* axis, $4p_z$ orbital mixing into the d_{z^2} orbital of a_1 symmetry is the dominant effect. The DFT calculation for the $[Fe(TMC)Cl]^+$ complex shows that the d_{z^2} orbital contains significant $4p_z$ character (7.4%), while the d_{xz} and d_{yz} e orbitals contained very little $4p_{xy}$ character (<0.1%). Thus, the transition to the $^4B_2$ state (which contains the $(e)^2(a_1)^0(b_1)^1$ component) should dominate the pre-edge spectrum. This transition is not affected by CI with forbidden two-electron excited states and thus will not be subject to redistribution of its electric dipole intensity. This is consistent with the data which show a single high-intensity low-energy feature and a weak higher energy feature (see Figure 3B). The amount of $4p_z$ mixing into the d_{z^2} orbital can be estimated from the experimental data using the same relationships developed for the tetrahedral complexes (1.22 units/percent 4p character, *vide supra*). The total pre-edge intensity for [Fe(TMC)Cl](BF_4) is 12.9(0.2) (Table 1). If 3.9(0.5) units are attributed to the electric quadrupole transition, then 9.0(0.5) units originate from $4p_z$ (electric dipole-allowed) character in the d_{z^2} orbital. The amount of $4p_z$ mixing into the $3d_{z^2}$ orbital is therefore 9.0(0.5)/1.22(0.5) = 7.4(3.0)%; this value is in good agreement with the theoretically estimated amount of 4p character in the $^4B_2$ final state. In addition, the DFT results demonstrate that although group theory allows for 4p mixing into both the Fe

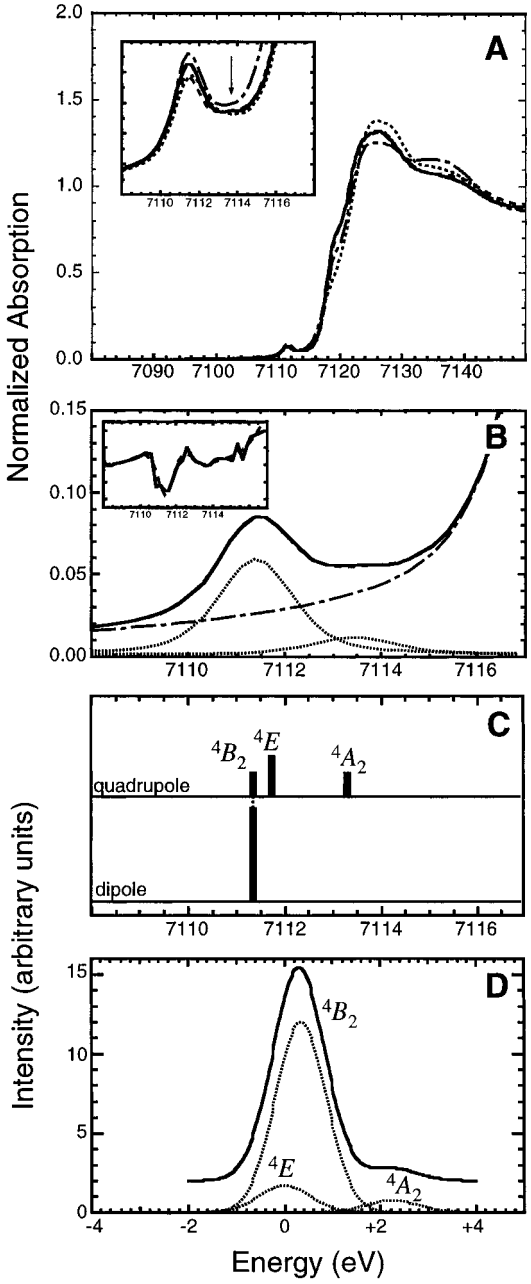

Figure 3. Fe K-edge XAS spectra, pre-edge fits, and theoretical analysis and simulation of five-coordinate square pyramidal high-spin Fe^{II} complexes. (A) Fe K-edge spectra of [Fe(TMC)Cl](BF$_4$) (—), [Fe(TMC)Br](BF$_4$) (- - -), [Fe(TMC)CH$_3$CN](BF$_4$)$_2$ (···), and [Fe(TMC)N$_3$](BF$_4$) (— -) where the inset is an expansion of the 1s → 3d pre-edge region with a normalized absorption scale of 0.0−0.1. (B) Fit to the Fe K-edge pre-edge region of [Fe(TMC)Cl](BF$_4$) including the experimental data (—), a fit to the data (- - -), the background function (— -), and the individual pre-edge peaks from the fit (···). The inset displays the second derivative of the data (—) and the second derivative of the fit to the data (- - -). (C) Theoretical energy splitting and intensity distribution in the $^4B_2$, ^4E, and $^4A_2$ final states through both the electric quadrupole and electric dipole intensity mechanisms. (D) Theoretical simulation of the pre-edge region for [Fe(TMC)Cl]$^+$ based upon single-determinant density functional solutions to the $^4B_2$, ^4E, and $^4A_2$ final states. The full simulated spectrum in shown as a solid line, with all component features shown as dotted lines.

$3d_{z^2}$ and $3d_{xz,yz}$ orbitals, significant mixing only occurs along the *z*-axis, explaining the experimental intensity distribution in the pre-edge.

Considering that only one final state gains intensity from the $4p_z$ mixing into the d_{z^2} orbital, the nature of the axial interaction should be reflected in the intensity and position of the most intense pre-edge feature. For example, the intensity of this pre-edge feature of the high-spin ferrous complexes in this study decreases as [Fe(TMC)N$_3$](BF$_4$) > [Fe(TMC)Cl](BF$_4$) > [Fe(TMC)CH$_3$CN](BF$_4$)$_2$ > [Fe(TMC)Br](BF$_4$). This trend matches the strength of the axial ligand, with the azide having the strongest interaction and bromide having the weakest.

Scheme 4

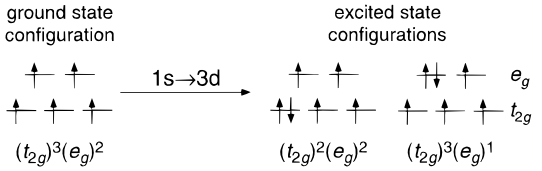

II. High-Spin Ferric Complexes. A. O_h Geometry. Fe K-edge XAS data were measured for a series of high-spin ferric octahedral model complexes with varying ligation: F^-, Cl^-, Br^-, and O and N from acac, malonate, oxalate, urea, and H_2O. The XAS edge spectra for FeF_3, $FeCl_3$, $FeBr_3$, and [$FeCl_6$][Co(NH_3)$_6$] are shown in Figure 4A, and the spectra for Fe(acac)$_3$, (NH_4)$_3$Fe(malonate)$_3$, [Fe(H_2O)$_6$](NH_4)(SO_4)$_2$·6H_2O, and Fe(urea)$_6$(ClO_4)$_3$ are shown in Figure 4B. The lowest energy transitions corresponding to K-edge excitation are the weak 1s → 3d pre-edge peaks, which are expanded and shown as insets in Figures 4A,B. All nine complexes have a low-intensity split pre-edge feature (Table 1). A fit to the pre-edge region of Fe(acac)$_3$ is shown in Figure 4C. The total pre-edge intensities of the octahedral high-spin ferric complexes range from 4.0 to 7.3, with the average intensity being 4.9. Note the large range of experimental intensities found in these octahedral ferric complexes.

Since all nine of these complexes have a centrosymmetric octahedral site, the only intensity mechanism available for the 1s → 3d feature is the allowed electric quadrupole transition. In the high-spin ferric d^5 case, the $^5A_{1g}$ ground state has a $(t_{2g})^3(e_g)^2$ configuration. Promotion of a 1s electron into the 3d manifold produces two excited hole configurations, $(t_{2g})^2(e_g)^2$ and $(t_{2g})^3(e_g)^1$ (Scheme 4).

Coupling of the holes in the $(t_{2g})^2(e_g)^2$ and $(t_{2g})^3(e_g)^1$ configurations gives a $^5T_2$ and a ^5E state, respectively.[90] Therefore, an octahedral high-spin ferric complex should show two pre-edge features split by an excited state 10*Dq* with an approximate electric quadrupole intensity ratio of 3:2. Fits to the data show that there are indeed two pre-edge features with an intensity ratio of ∼3:2 and splittings that range from 1.1 to 1.5 eV (Figure 4C and Table 1). Deviations from the predicted 3:2 intensity ratio of the two features should reflect differences in covalency. The e_g set of the 3d orbitals is more covalent than the t_{2g} set due to σ bonding interactions with the ligands, and thus, states containing a $(t_{2g})^2(e_g)^2$ component should be more intense than states containing a $(t_{2g})^3(e_g)^1$ component. Density functional calculations on $[FeCl_6]^{3-}$ indicate that the ^5E_g final state acceptor orbitals have much less Fe 3d character (50% Fe 3d) than the acceptor orbitals in the $^5T_{2g}$ final state (76% Fe 3d). Thus, the $^5T_{2g}$:^5E_g intensity ratio will favor the $^5T_{2g}$ final state (see parts D (middle) and E of Figure 4).

The energy splitting between the two pre-edge features is a direct probe of the magnitude of 10*Dq* in the $d^{(n+1)}$ final state. In comparing these energy splittings with ground state 10*Dq* values from optical data,[94] the excited state 10*Dq* values are about 80% of the ground state values. The splitting of the two pre-edge features in these complexes can be related to ligand field strength, with the splittings following the trend Fe−O/Fe−N > FeF_3 > $FeCl_3$ > $FeBr_3$. The increase of the splitting of the two pre-edge features with increased ligand field strength is exemplified in Figure 4D.

B. T_d Geometry. Fe K-edge XAS data were measured for (Et_4N)[$FeCl_4$], a high-spin ferric tetrahedral complex. Its XAS

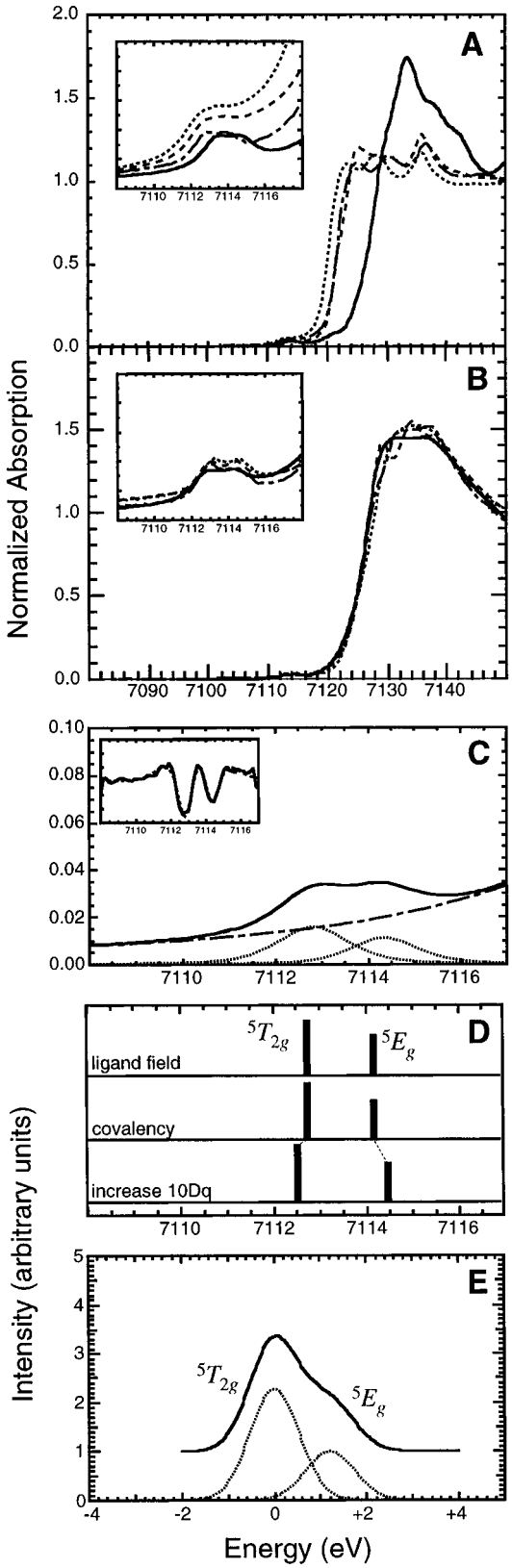

Figure 4. Fe K-edge XAS spectra, pre-edge fits, and theoretical analysis and simulation of octahedral high-spin Fe^{III} complexes. Fe K-edge spectra of (A) FeF_3 (—), $FeCl_3$ (- - -), $FeBr_3$ (•••), and $[FeCl_6]$-$[Co(NH_3)_6]$ (— -) and (B) $Fe(acac)_3$ (—), $(NH_4)_3Fe(malonate)_3$ (- - -), $[Fe(H_2O)_6](NH_4)(SO_4)_2 \cdot 6H_2O$ (•••), and $Fe(urea)_6(ClO_4)_3$ (— -). The insets are expansions of the 1s → 3d pre-edge region with the normalized absorption scaled from 0.0 to 0.1 in each case. (C) Fit to the Fe K-edge pre-edge region of $Fe(acac)_3$ including the experimental data (—), a fit to the data (- - -), the background function (— -), and the individual pre-edge peaks from the fit (•••). The inset displays the second derivative of the data (—) and the second derivative of the fit to the data (- - -). (D) Systematic analysis of the octahedral pre-edge features including the effect of the ligand field on the electric quadrupole intensity, the effects due to covalency, and the behavior of the pre-edge region with increasing 10*Dq*. (E) Theoretical simulation of the pre-edge region for $[FeCl_6]^{3-}$ based on density functional solutions for the $^5T_{2g}$ and ^5E_g final states. The full simulated spectrum in shown as a solid line, with all component features shown as dotted lines.

Scheme 5

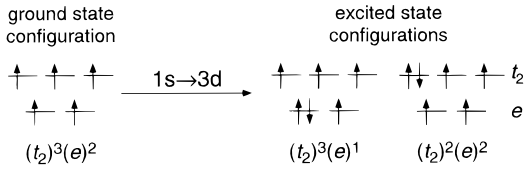

spectrum is shown in Figure 5 with the 1s → 3d pre-edge region expanded in the inset. $(Et_4N)[FeCl_4]$ has a very intense single pre-edge feature (Table 1). A fit to the pre-edge region is shown in Figure 5B.

The 1s → 3d pre-edge feature of $(Et_4N)[FeCl_4]$ gains intensity both through the allowed electric quadrupole mechanism and from the electric dipole mechanism associated with 4p mixing into the 3d orbitals. As in the high-spin ferric octahedral case, there are two one-electron allowed excited hole configurations, $(t_2)^2(e)^2$ and $(t_2)^3(e)^1$ (Scheme 5), that produce two many-electron states, $^5T_2$ and ^5E, respectively.

Consequently, a tetrahedral high-spin ferric complex can have a transition to the doubly degenerate ^5E state and also to a triply degenerate $^5T_2$ state 10*Dq* higher in energy. Energies of the many-electron states were calculated with the $d^{(n+1)} = d^6$ Tanabe−Sugano matrices using a 10*Dq* value of 5200 cm^{-1} (80% of the ground state 10*Dq* of $(Et_4N)[FeCl_4]$)[104], a *B* value of 950 cm^{-1} (90% of the $d^{(n+1)}$ *B*), and a *C* value of 3800 cm^{-1}. Using these values, the energy splitting between the ^5E and $^5T_2$ states is 0.6 eV (Figure 5C, top) which should not be resolvable at the Fe K-edge.

The pre-edge features should also gain intensity from 4p mixing into the 3d orbitals. The 4p orbitals transform as t_2 so there is only mixing into the 3d t_2 set which contributes to the intensity of the transition into the $^5T_2$ state (see Figure 5C). If the total electric quadrupole intensity is 4.9(1.0) as determined from the octahedral ferric complexes, the experimental electric dipole intensity for $(Et_4N)[FeCl_4]$ is 15.8(1.3). In the case of ferric complexes, the 1s → 4p oscillator strength (eq 1) is 0.83 and the correction for the 1s → continuum normalization is 129% relative to Cu(II). From this, 1.50(0.6) units of intensity represent 1% 4p character in the 3d manifold. The total amount of 4p mixing into the t_2 orbitals observed experimentally is thus calculated to be 10.3(4.1)%. DFT calculations on $[FeCl_4]^-$ indicate ∼2.5% 4p mixing into each of the t_2 orbitals, giving a total of 7.5% 4p character in the pre-edge features and giving a reasonable estimate for the overall intensity distribution over the XAS final states.

C. C_{4v} Geometry. Fe K-edge data were collected for Fe(salen)Cl, a square pyramidal high-spin ferric complex. The XAS spectrum of Fe(salen)Cl is shown in Figure 6A with the pre-edge region expanded and shown in the inset. The pre-edge feature of Fe(salen)Cl appears to consist of an intense low-energy feature with a much weaker high-energy feature (Table 1). A fit to the pre-edge region is shown in Figure 6B.

The C_{4v} site is noncentrosymmetric, and thus the 1s → 3d pre-edge transition can gain intensity from both the allowed electric quadrupole transition and 4p mixing into the 3d orbitals, giving electric dipole intensity. The C_{4v} site is treated as a distorted O_h site, in which the $d^{(n+1)}$ $^5T_2$ state splits into a $^5B_2$ and a ^5E state and the ^5E state splits into a $^5A_1$ and a $^5B_1$ state.

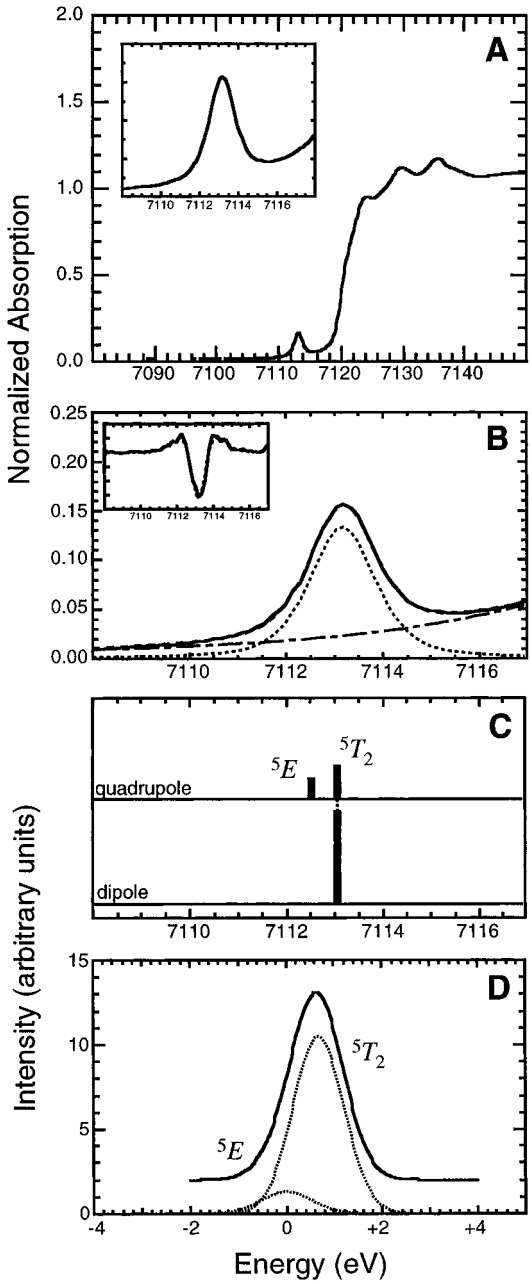

Figure 5. Fe K-edge XAS spectra, pre-edge fits, and theoretical analysis and simulation of a tetrahedral high-spin Fe^{III} complex. (A) Fe K-edge spectrum of $(Et_4N)[FeCl_4]$ (—) where the inset is an expansion of the 1s → 3d pre-edge region with a normalized absorption scale of 0.0−0.2. (B) Fit to the Fe K-edge pre-edge region of (Et_4N)-$[FeCl_4]$ including the experimental data (—), a fit to the data (- - -), the background function (— -), and the individual pre-edge peak from the fit (···). The inset displays the second derivative of the data (—) and the second derivative of the fit to the data (- - -). (C) Theoretical energy splitting and intensity distribution in the ^5E and $^5T_2$ final states through both the electric quadrupole and electric dipole intensity mechanisms. (D) Theoretical simulation of the pre-edge region for $[FeCl_4]^-$ based on density functional calculations for the ^5E and $^5T_2$ final states. The full simulated spectrum in shown as a solid line, with all component features shown as dotted lines.

These correspond to the four one-electron allowed excited hole configurations shown in Scheme 6.

The relative energies of the excited states associated with these configurations can be determined from density functional calculations and from experimental observations of the 3d orbital energies.[94] From the calculations, the $(b_2)^0(e)^2(a_1)^1(b_1)^1$ configuration (which comprises the $^5B_2$ final state) is lowest in energy, followed by the $(b_2)^1(e)^1(a_1)^1(b_1)^1$ configuration (^5E final state) at 0.3 eV, the $(b_2)^1(e)^1(a_1)^0(b_1)^1$ configuration ($^5A_1$ final state) at 1.1 eV, and finally the $(b_2)^1(e)^2(a_1)^1(b_1)^0$ configuration ($^5B_1$ final state) at 2.1 eV. The electric quadrupole intensity into these states should have an approximate intensity ratio of 1:2:1:1 (see Figure 6C).

Scheme 6

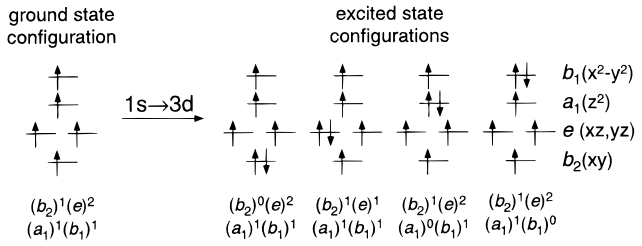

The pre-edge features of square pyramidal complexes gain additional intensity from 4p mixing into the 3d orbitals due to the noncentrosymmetric ligand field at the metal site. As previously described for the ferrous C_{4v} complexes, the 4p orbitals transform as e ($4p_{x,y}$) and a_1 ($4p_z$). The axial distortion along the *z*-axis is expected to yield strong mixing of the $4p_z$ with the $3d_{z^2}$ orbital; in contrast, the 4p orbitals of e symmetry should not mix significantly with the 3d orbitals due to minimal distortion in the equatorial plane. Electric dipole character should only be observable into the $^5A_1$ final state as it corresponds to the 1s → $3d_{z^2}$ (+$4p_z$) transition. This is consistent with the pre-edge data which show an intense low-energy feature corresponding to the unresolved transitions into the $^5B_2$, ^5E, and $^5A_1$ final states (with electric dipole intensity into the $^5A_1$ state) and a weak higher energy feature corresponding to the $^5B_1$ final state. Calculations on a model for Fe(salen)Cl indicate that the $3d_{z^2}$ orbital contains significant $4p_z$ character (6.6%), but has no observable mixing between the $3d_{xz,yz}$ and $4p_{x,y}$ orbitals (<0.1%). The amount of $4p_z$ mixing into the d_{z^2} orbital is estimated experimentally from the total pre-edge intensity of the Fe(salen)Cl complex. If 4.9(1.0) total units of intensity (average for the octahedral ferric complexes) are attributed to electric quadrupole intensity, then 9.5(1.2) units come from $4p_z$ (electric dipole-allowed) character in the d_{z^2} orbital. The relationship between intensity and 4p character is the same as for the ferric tetrahedral complexes; therefore, the amount of $4p_z$ mixing into the d_{z^2} orbital is estimated to be 9.5(1.2)/1.5(0.6) = 6.3(2.5)%. As in the high-spin ferrous square pyramidal case, only one state ($^5A_1$) gains intensity from 4p mixing; thus, the intensity and position of the most intense pre-edge feature will reflect the nature of the axial interaction in the complex.

III. Binuclear Complexes. Fe K-edge data were measured for a series of binuclear iron model complexes with varying oxidation states, geometries, and bridging ligation. The complexes studied are listed in Table 2. Figure 7 displays XAS spectra of representative complexes with the insets containing

(72) Feng, X.; Bott, S. G.; Lippard, S. J. *J. Am. Chem. Soc.* **1989**, *111*, 8046.
(73) Tolman, W. B.; Bino, A.; Lippard, S. J. *J. Am. Chem. Soc.* **1989**, *111*, 8522.
(74) Armstrong, W. H.; Spool, A.; Papaefthymiou, G. C.; Frankel, R. B.; Lippard, S. J. *J. Am. Chem. Soc.* **1984**, *106*, 3653.
(75) Armstrong, W. H.; Lippard, S. J. *J. Am. Chem. Soc.* **1984**, *106*, 4632.
(76) Thich, J. A.; Ou, C. C.; Powers, D.; Vasiliou, B.; Mastropaolo, D.; Potenza, J. A.; Schugar, H. J. *J. Am. Chem. Soc.* **1976**, *98*, 1425.
(77) Snyder, B. S.; Patterson, G. S.; Abrahamson, A. J.; Holm, R. H. *J. Am. Chem. Soc.* **1989**, *111*, 5214.
(78) Norman, R. E.; Yan, S.; Que, L., Jr.; Backes, G.; Ling, J.; Sanders-Loehr, J.; Zhang, J. H.; O'Connor, C. J. *J. Am. Chem. Soc.* **1990**, *112*, 1554.
(79) Norman, R. E.; Holz, R. C.; Ménage, S.; O'Connor, C. J.; Zhang, J. H.; Que, L., Jr. *Inorg. Chem.* **1990**, *29*, 4629.

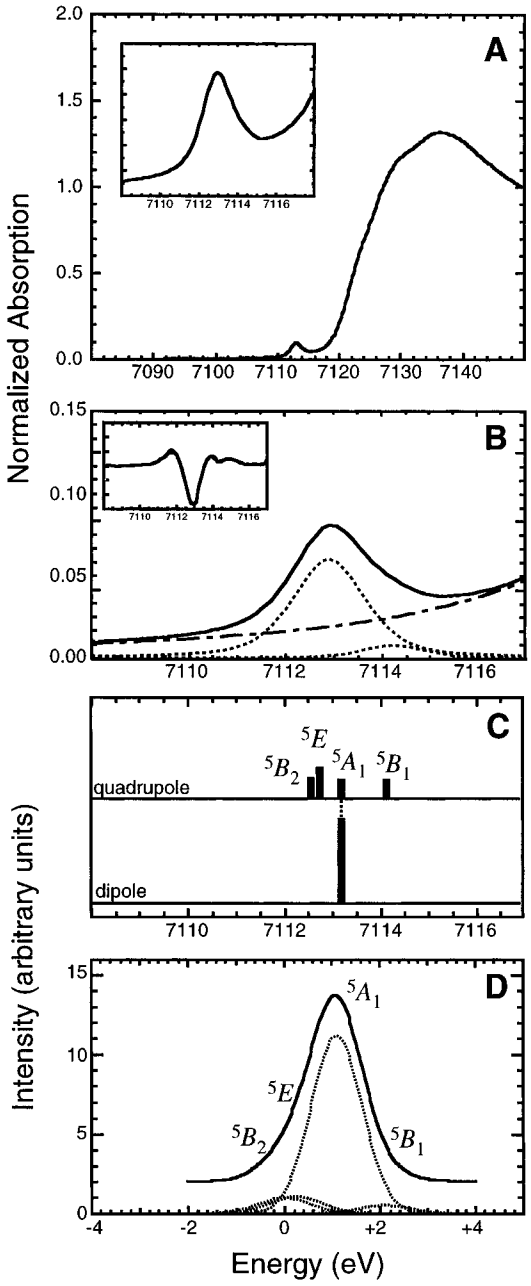

Figure 6. Fe K-edge XAS spectra, pre-edge fits, and theoretical analysis and simulation of a five-coordinate square pyramidal high-spin Fe^{III} complex. (A) Fe K-edge spectrum of Fe(salen)Cl (—) where the inset is an expansion of the 1s → 3d pre-edge region with a normalized absorption scale of 0.00−0.12. (B) Fit to the Fe K-edge pre-edge region of Fe(salen)Cl including the experimental data (—), a fit to the data (- - -), the background function (— -), and the individual pre-edge peaks from the fit (···). The inset displays the second derivative of the data (—) and the second derivative of the fit to the data (- - -). (C) Theoretical energy splitting and intensity distribution in the $^5B_2$, ^5E, $^5A_1$, and $^5B_1$ final states through both the electric quadrupole and electric dipole intensity mechanisms. (D) Theoretical simulation of the pre-edge region for [Fe(salen)Cl] based on density functional calculations of the $^5B_2$, ^5E, $^5A_1$, and $^5B_1$ final states. The full simulated spectrum in shown as a solid line, with all component features shown as dotted lines.

an expanded view of the 1s → 3d pre-edge region. Figure 7A shows a comparison of spectra of a six- and a five-coordinate diferrous complex, $(Et_4N)_2[Fe_2(salmp)_2]\cdot 2DMF$ and $[Fe_2(OBz)(et\text{-}HPTB)](BF_4)_2$, to those of a six- and a five-coordinate monomeric complex. $(Et_4N)_2[Fe_2(salmp)_2]\cdot 2DMF$, with two six-coordinate ferrous centers with O and N ligation,[77] has a low-intensity pre-edge feature that is split by ~2 eV, very similar to the results obtained for monomeric six-coordinate ferrous complexes with similar coordination (see Figure 1B). Fits to the pre-edge region of the dimer yield three peaks with peak energies and intensities that are consistent with the monomer data (Tables 1 and 2). $[Fe_2(OBz)(et\text{-}HPTB)](BF_4)_2$ has two five-coordinate ferrous sites[82] and also has a split pre-edge feature; however, the lower energy feature is much more intense, similar to that of monomeric C_{4v} ferrous complexes (Figure 7A; Tables 1 and 2). Figure 7B shows an analogous comparison of a six- and a four-coordinate diferric complex, $[Fe_2OH(OAc)_2(HB(pz)_3)_2](ClO_4)$ and $(BzPHMe_2N)_2[Fe_2OCl_6]$, with those of the corresponding six- and four-coordinate monomeric complexes. $[Fe_2OH(OAc)_2(HB(pz)_3)_2](ClO_4)$ has two near-octahedral six-coordinate sites[75] and a low-intensity pre-edge feature that is split, similar to that of the monomeric ferric complex. $(BzPHMe_2N)_2[Fe_2OCl_6]$ contains ferric sites with three chloride ligands and a μ-oxo bridge in an approximately tetrahedral geometry.[83] The dimer exhibits a single very intense pre-edge feature, similar to that of monomeric tetrahedral ferric complexes but with somewhat greater intensity. This intensity gain reflects the increased distortion of the site from the short μ-oxo bridging ligand.

From the above similarities in pre-edge features between monomeric and dimeric complexes of similar oxidation state, ligation, and geometry, we can conclude that the pre-edge splittings and intensities predicted from atomic multiplet theory can be used to explain dimeric as well as monomeric iron complexes.

Spectra of $[Fe_2OH(OAc)_2(HB(pz)_3)_2](ClO_4)$, $[Fe_2O(OAc)_2(HB(pz)_3)_2]$, $[Fe_2(TPA)_2O(OAc)](ClO_4)_2$, and $(enH_2)[Fe_2O(HEDTA)_2]\cdot 6H_2O$ are shown in Figure 7C. All four of these complexes are diferric with varying bridging ligands. The first two have the same ligand set with the exception of the former having a hydroxide bridge, while the latter has a μ-oxo bridge. The hydroxide-bridged complex has only a weak, split pre-edge feature while the μ-oxo-bridged complex has a much more intense higher energy feature with a lower energy shoulder. $[Fe_2(TPA)_2O(OAc)](ClO_4)_2$ and $(enH_2)[Fe_2O(HEDTA)_2]\cdot 6H_2O$ each have a μ-oxo bridge, with the former having an additional acetate bridge. Both of these complexes show a pre-edge feature similar to that of $[Fe_2O(OAc)_2(HB(pz)_3)_2]$. In fact, *all* of the dimer complexes studied which contained a μ-oxo bridging ligand had a distinctive pre-edge feature characterized by a higher energy intense feature and a lower energy shoulder (inset of Figure 7C and Table 2). Thus, the μ-oxo bridge seems to have a dominant effect on the pre-edge features, as mono-, di-, and tribridged complexes that contain a μ-oxo bridge all have very similar pre-edge features.

As mentioned above, there is also a striking difference in the pre-edge feature of hydroxide- *vs* μ-oxo-bridged complexes, as can be seen in the pre-edge features of $[Fe_2OH(OAc)_2(HB(pz)_3)_2](ClO_4)$ and $[Fe_2O(OAc)_2(HB(pz)_3)_2]$ (Figure 7C). The six-coordinate μ-oxo-bridged dimers can be viewed as having an iron site with C_{4v} symmetry similar to the five-coordinate ferric complexes but with the axial ligand having a larger ligand field strength since the O of the μ-oxo bridge has moved closer to the iron site. This shortening of the axial bond strongly perturbs the iron site, allowing for 4p mixing into the 3d orbitals and for splitting of the 3d orbitals, with a strong ligand field along the *z*-axis. As discussed above for the high-spin ferric

(80) Gaines, A., Jr.; Hammett, L. P.; Walden, G. H., Jr. *J. Am. Chem. Soc.* **1936**, *58*, 1668.
(81) Lippard, S. J.; Schugar, H.; Walling, C. *Inorg. Chem.* **1967**, *6*, 1825.
(82) Dong, Y.; Ménage, S.; Brennan, B. A.; Elgren, T. E.; Jang, H. G.; Pearce, L. L.; Que, L., Jr. *J. Am. Chem. Soc.* **1993**, *115*, 1851.
(83) Neuse, E. W.; Khan, F. B. D.; Berhalter, K.; Thewalt, U. *J. Cryst. Spectrosc. Res.* **1986**, *16*, 483.

Table 2. XAS Pre-Edge Energies and Intensities for Binuclear Iron Model Complexes

compound	oxidation state	ligation	beamline, temperature	pre-edge peak energy[a]	pre-edge peak int[a,b]	total pre-edge peak int[b]	peak energy difference[c]	peak int ratio[d]	ref
$[Fe_2O(OAc)_2\{[OP(OEt)_2]_3Co(C_2H_5)\}_2]$	diferric	6 O *O, (OAc)$_2$*	NSLS X19A,10 K	7112.81(0.13) 7114.25(0.06)	3.3(1.0) 10.6(1.9)	13.9(1.0)	1.4	0.24	72
$[Fe_2O(O_2CH)_4(BIPhMe_2)](CH_3OH)$	diferric	4 O, 2 N *O, (O$_2$CH)$_2$*	SSRL 4-3,10 K	7112.92(0.08) 7114.64(0.02)	4.0(0.7) 10.9(1.3)	14.9(0.7)	1.7	0.27	73
$[Fe_2O(OAc)_2(HB(pz)_3)_2]$	diferric	3 O, 3 N *O, (OAc)$_2$*	SSRL 7-3,300 K	7112.68(0.05) 7114.35(0.01)	4.1(0.5) 12.5(1.1)	16.6(0.7)	1.7	0.25	74
$[Fe_2OH(OAc)_2(HB(pz)_3)_2](ClO_4)$	diferric	3 O, 3 N *OH,(OAc)$_2$*	SSRL 7-3,300 K	7112.68(<0.01) 7114.35(0.01)	3.2(0.2) 2.3(0.2)	5.5(0.4)	1.7	0.57	75
$[FeOH(H_2O)Chel]_2(H_2O)_4$	diferric	5 O, 1 N *(OH)$_2$*	SSRL 7-3,300 K	7112.88(0.02) 7114.28(0.03)	5.8(0.4) 2.7(0.4)	8.5(0.3)	1.4	0.68	76
$[FeOH(H_2O)Dipic]_2$	diferric	5 O, 1 N *(OH)$_2$*	SSRL 4-2,10 K	7112.89(0.02) 7114.30(0.04)	5.1(0.6) 2.3(0.2)	7.4(0.6)	1.4	0.69	76
$[Fe_2(salmp)_2]\cdot 2DMF$	diferric	4 O, 2 N *(OPh)$_2$*	SSRL 7-3,10 K	7112.51(0.01) 7114.06(0.02)	3.6(0.2) 3.8(0.2)	7.4(0.2)	1.6	0.49	77
$(Et_4N)[Fe_2(salmp)_2]\cdot 2DMF$	semimet	4 O, 2 N *(OPh)$_2$*	SSRL 7-3,10 K	7111.37(0.12) 7112.54(0.04) 7114.03(0.02)	0.9(0.5) 4.5(0.7) 1.0(0.2)	6.4(0.3)	2.7	0.85	77
$(Et_4N)_2[Fe_2(salmp)_2]\cdot 2DMF$	diferrous	4 O, 2 N *(OPh)$_2$*	SSRL 7-3,10 K	7111.44(0.04) 7112.35(0.07) 7113.57(0.04)	2.7(0.2) 0.8(0.3) 1.4(0.1)	5.0(0.3)	2.1	0.71	77
$[Fe_2(TPA)_2O(OAc)](ClO_4)_2$	diferric	2 O, 4 N *O, OAc*	SSRL 7-3,300 K	7112.51(0.08) 7114.21(0.01)	3.4(0.4) 11.6(2.1)	14.9(1.7)	1.7	0.22	78
$[Fe_2(TPA)_2O(CO_3)](ClO_4)_2$	diferric	2 O, 4 N *O, CO$_3$*	SSRL 7-3,300 K	7112.55(0.06) 7114.11(0.01)	3.1(0.3) 11.5(2.0)	14.6(1.8)	1.6	0.21	79
$[Fe_2(TPA)_2O(phthalate)](ClO_4)_2$	diferric	2 O, 4 N *O, OPht*	SSRL 7-3,300 K	7112.44(0.06) 7114.18(0.02)	3.5(0.3) 11.5(2.1)	15.0(1.9)	1.7	0.23	79
$[Fe_2O(phen)_4(H_2O)_2](ClO_4)_4$	diferric	2 O, 4 N *O*	SSRL 4-2,10 K	7112.58(0.03) 7114.37(0.02)	3.0(0.3) 10.2(0.6)	13.2(0.8)	1.8	0.23	80
$(enH_2)[Fe_2O(HEDTA)_2]\cdot 6H_2O$	diferric	4 O, 2 N *O*	SSRL 7-3,10 K	7112.76(0.04) 7114.29(0.02)	2.9(0.5) 7.6(0.5)	10.5(0.6)	1.5	0.28	81
$[Fe_2(OBz)(et\text{-}HPTB)](BF_4)_2$	diferrous	2 O, 3 N *alkoxo,OBz*	SSRL 7-3,10 K	7111.68(0.01) 7113.41(0.01)	10.9(0.2) 2.2(0.1)	13.0(0.3)	1.7	0.83	82
$(BzPhMe_2N)_2[Fe_2OCl_6]$	diferric	1 O, 3 Cl *O*	SSRL 2-3,10 K	7113.37(0.01)	27.1(1.2)	27.1(1.2)			83

[a] Bridging ligands are denoted by italics. [b] Pre-edge energies and intensities were determined by fits to the data (see the Experimental Section for details on the fitting procedure). [c] The values reported for the pre-edge intensities were multiplied by 100. [d] Peak energy differences are the energy differences between the lowest energy and the highest energy pre-edge features. [e] Peak intensity ratios are the intensity of the first pre-edge feature divided by the total pre-edge intensity (all discrepencies are attributable to roundoff in the reporting of peak intensities).

C_{4v} case, the 4p orbitals transform as e and a_1, and if the main distortion is along the *z* axis, the dominant effect will be that of the $4p_z$ orbital (a_1) mixing into the d_{z^2} orbital. In this model, the transition to the $^5A_1$ state that contains the $(b_2)^1(e)^2(a_1)^0(b_1)^1$ component (Scheme 6) should be the most intense. Due to the increased ligand repulsion along the oxo *z*-axis, the d_{xz}, d_{yz}, and d_{z^2} orbitals will increase in energy with respect to the d_{xy} and $d_{x^2-y^2}$ orbitals. This effect increases the energy of the $^5A_1$ state so that it is the highest energy state. Thus, the higher energy pre-edge feature should be the most intense. This explains the distinctive shape of all the μ-oxo-bridged complexes (Figure 7C and Table 2) and their similarity to the C_{4v} five-coordinate monomers except that the electric dipole-allowed transition to the $^5A_1$ has shifted to higher energy due to the strong rather than weak interactions with the oxo bridging ligand.

The amount of $4p_z$ mixing can be estimated. The total pre-edge peak intensities for all the octahedral ferric dimers with μ-oxo bridges range from 10.5 to 16.6 (Table 2), with the average total peak intensity being 14.2. Subtracting the total electric quadrupole intensity of 4.9 (average from the octahedral ferric complexes) gives an electric dipole intensity of 9.3. Using the intensity relationship derived for ferric complexes, the amount of $4p_z$ mixing into the d_{z^2} orbital is $9.3/1.5 \approx 6.2\%$.

IV. Low-Spin Iron Complexes. A. Ferrous Complexes. Fe K-edge XAS data were obtained for the following low-spin ferrous complexes: $Fe(HB(pz)_3)_2$, $Fe(prpep)_2$, and $K_4[Fe(CN)_6]\cdot 3H_2O$. XAS spectra for these three complexes are shown in Figure 8A, with the inset showing an expanded view of the 1s → 3d pre-edge region. All three complexes have a weak, single pre-edge feature, with the feature of $Fe(HB(pz)_3)_2$ being the lowest in energy and that of $K_4[Fe(CN)_6]\cdot 3H_2O$ being highest in energy (Table 3). A fit to the pre-edge region of $Fe(prpep)_2$ is shown in Figure 8B.

All three low-spin ferrous complexes have an octahedral iron site, and therefore, the only intensity mechanism for the 1s → 3d pre-edge feature is the allowed electric quadrupole

(84) Trofimenko, S. *J. Am. Chem. Soc.* **1967**, *89*, 3170.
(85) Oliver, J. D.; Mullica, D. F.; Hutchinson, B. B.; Milligan, W. O. *Inorg. Chem.* **1980**, *19*, 165.
(86) Brown, S. J.; Olmstead, M. M.; Mascharak, P. K. *Inorg. Chem.* **1990**, *29*, 3229.
(87) Wyckoff, R. W. G. *Crystal Structures*, 2nd ed.; Robert E. Krieger Publishing Co.: Malabar, FL, 1982; Vol. 3, pp 687, 702.
(88) Rosenzweig, A. C.; Lippard, S. J. Private communication, 1992.
(89) Figgis, B. N.; Skelton, B. W.; White, A. H. *Aust. J. Chem.* **1978**, *31*, 1195.
(90) Griffith, J. S. *The Theory of Transition Metal Ions*; Cambridge University Press: Cambridge, 1961.
(91) de Groot, F. M. F. *J. Electron Spectrosc. Relat. Phenom.* **1994**, *67*, 529.
(92) Sugano, S.; Tanabe, Y.; Kamimura, H. *Multiplets of Transition-Metal Ions in Crystals*; Academic Press: New York, 1970.
(93) Karshipin, T. B.; Gebhard, M. S.; Solomon, E. I.; Raymond, K. N. *J. Am. Chem. Soc.* **1991**, *113*, 2977.
(94) Lever, A. B. P. *Inorganic Electronic Spectroscopy*, 2nd ed.; Elsevier: Amsterdam, 1984.
(95) The relative intensity is given by the coefficient of the one-electron allowed configuration in the state summed over the number of allowed one-electron transitions to that configuration divided by the ground state degeneracy.
(96) Furlane, E.; Cervone, E.; Valent, V. *J. Nucl. Chem.* **1963**, *25*, 159.
(97) Gewirth, A. A.; Cohen, S. L.; Schugar, H. J.; Solomon, E. I. *Inorg. Chem.* **1987**, *26*, 1133.

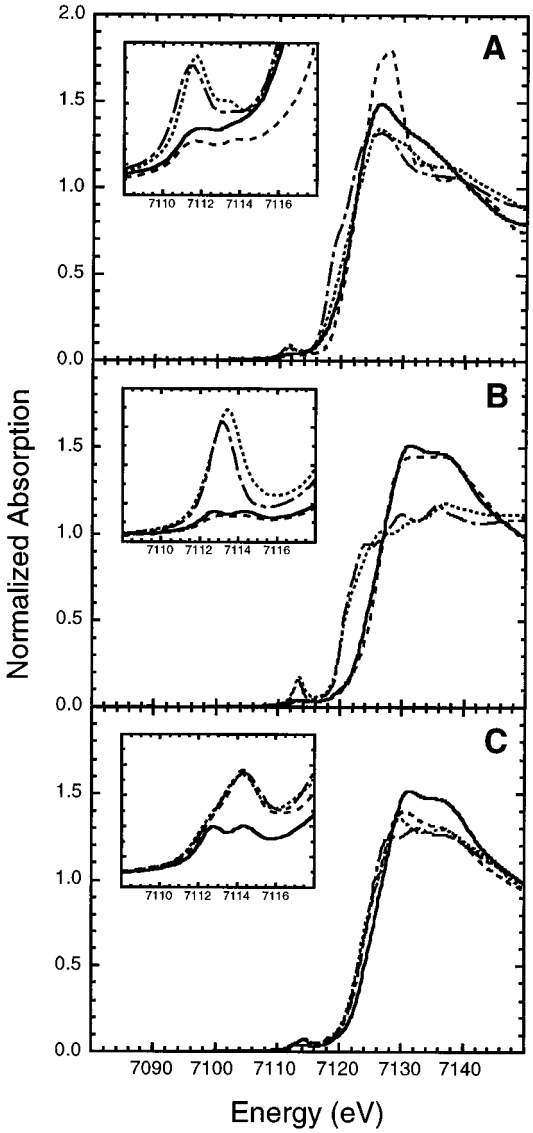

Figure 7. Comparison of Fe K-edge XAS spectra of binuclear iron complexes with their analogous monomeric species. Fe K-edge spectra of (A) $(Et_4N)_2[Fe_2(salmp)_2]\cdot 2DMF$ (—), $[Fe(H_2O)_6][SiF_6]$ (- - -), $Fe_2(OBz)(et\text{-}HPTB)](BF_4)_2$ (···),and $[Fe(TMC)Cl](BF_4)$ (— -), (B) $[Fe_2OH(OAc)_2(HB(pz)_3)_2)](ClO_4)$ (—), $Fe(acac)_3$ (- - -), $(BzPHMe_2N)_2[Fe_2OCl_6]$ (···), and $(Et_4N)[FeCl_4]$ (— -), and (C) $[Fe_2OH(OAc)_2(HB(pz)_3)_2)](ClO_4)$ (—), $[Fe_2O(OAc)_2(HB(pz)_3)_2)]$ (- - -), $[Fe_2(TPA)_2O(OAc)](ClO_4)_2$ (···), and $(enH_2)[Fe_2O(HEDTA)_2]\cdot 6H_2O$ (— -). The insets in (A), (B), and (C) are expansions of the 1s → 3d pre-edge region, with the normalized absorption scales being 0.0−0.1 in (A) and (C) and 0.0−0.2 in (B).

transition. The $^1A_{1g}$ ground state of these low-spin ferrous complexes has an electronic hole configuration of $(e_g)^4$, with $(e_g)^3$ being the only allowed excited hole configuration (Scheme 7). The $(e_g)^3$ hole configuration produces a ^2E_g excited many-electron state. A transition into the ^2E_g state gives rise to a single pre-edge feature (Figure 8C and Table 3). The average total pre-edge intensities for these low-spin complexes is 4.6, which is similar to that of the high-spin ferrous complexes. A feature on the rising edge of the spectrum at ∼7115.5 eV is also observed. For this feature at ∼3.5 eV above the pre-edge to arise from a transition to the 3d manifold, significant (10−15%) configurational mixing between the one-electron allowed ^2E_g state and higher energy two-electron ^2E_g excited states would be necessary. Ligand field theory predicts only 2% mixing of the one-electron allowed final state with states at higher energy (∼5 and 7 eV above the one-electron allowed ^2E_g). This feature is therefore not a 1s → 3d feature and is assigned as an edge transition.

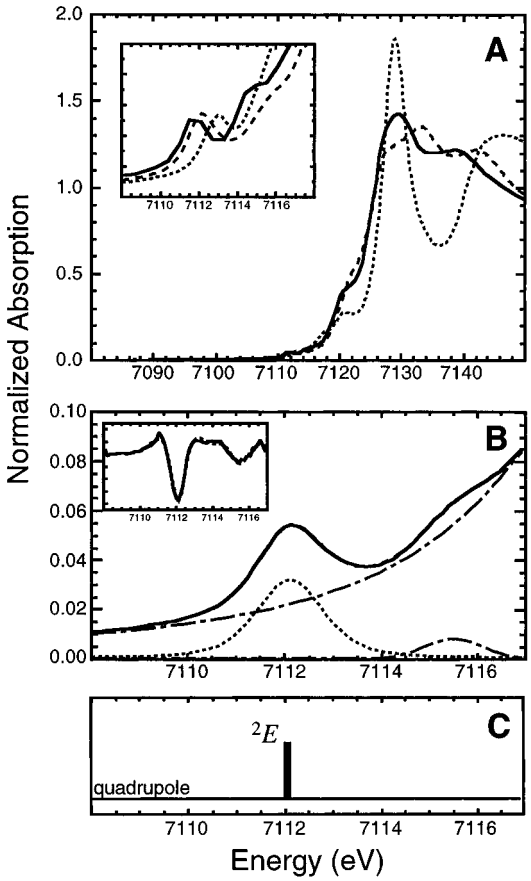

Figure 8. Fe K-edge XAS spectra, pre-edge fits, and theoretical analysis of octahedral low-spin Fe^{II} complexes. (A) Fe K-edge spectra of $Fe(HB(pz)_3)_2$ (—), $Fe(prpep)_2$ (- - -), and $K_4[Fe(CN)_6]\cdot 3H_2O$ (···) where the inset is an expansion of the 1s → 3d pre-edge region, with the normalized absorption scale being 0.0−0.1. (B) Fit to the Fe K-edge pre-edge region of $Fe(prpep)_2$ including the experimental data (—), a fit to the data (- - -), the background function (— -), and the individual pre-edge peak from the fit (···). An edge peak was also needed in the fit of this data and is shown (— -; see the text). The inset displays the second derivative of the data (—) and the second derivative of the fit to the data (- - -). (C) The single many-electron $d^{(n+1)}$ excited state.

B. Ferric Complexes. Fe K-edge XAS data were obtained for the low-spin ferric complexes $[Fe(HB(pz)_3)_2](ClO_4)$, $[Fe(prpep)_2](ClO_4)$, and $K_3[Fe(CN)_6]$. XAS spectra for these three complexes are shown in Figure 9A with an expanded view of the 1s → 3d pre-edge region shown in the inset. All three of these complexes have a weak pre-edge feature with a shoulder at lower energy. A very weak higher energy shoulder is also present, but difficult to resolve due to the onset of the edge features. The splitting between the lower energy shoulder and

(98) Shadle, S. E.; Penner-Hahn, J. E.; Schugar, H. J.; Hedman, B.; Hodgson, K. O.; Solomon, E. I. *J. Am. Chem. Soc.* **1993**, *115*, 767.

(99) Verner, D. A.; Yakovlev, D. G. *Astron. Astrophys. J.* **1995**, *109*, 125.

(100) Normalization for the Cu(II) complex was done at 9000 eV (see ref 98). Cross sections were calculated from analytic fits for the oscillator strength for the photoionization of a 1s electron.

(101) The oscillator strength is proportional to the square of the transition moment integral for the transition.

(102) In the limit, $Z_{1s} = Z$ due to minimal shielding by electrons in higher electronic shells ($Z_{1s}(Cu^{II}) = 29$, $Z_{1s}(Fe^{II}) = 26$). Z_{3d} was calculated using Slater's rules for the $d^{(n+1)}$ valence configuration ($Z_{3d}(Cu^{II}) = 7.85$, $Z_{3d}(Fe^{II}) = 5.90$).

(103) Karplus, M.; Porter, R. N. *Atoms and Molecules*; W. A. Benjamin, Inc.: London, 1970; p 228.

(104) Deaton, J. C.; Gebhard, M. S.; Solomon, E. I. *Inorg. Chem.* **1989**, *28*, 877.

Table 3. XAS Pre-Edge Energies and Intensities for Low-Spin Iron Model Complexes

compound	oxidation state	ligation	beamline, temperature	pre-edge peak energy[a]	pre-edge peak int[a,b]	total pre-edge peak int[b]	peak energy difference[c]	peak int ratio[d]	ref
$Fe(HB(pz)_3)_2$	ferrous	6 N	NSLS X19A, 10 K	7111.70(0.03)	4.2(0.2)	4.2(0.2)			84, 85
$Fe(prpep)_2 \cdot 2CH_3OH$	ferrous	6 N	SSRL 7-3,10 K	7112.12(0.01)	5.3(0.2)	5.3(0.2)			86
$K_4[Fe(CN)_6] \cdot 3H_2O$	ferrous	6 C	SSRL 7-3,10 K	7112.85(0.01)	4.2(0.4)	4.2(0.4)			87
$[Fe(HB(pz)_3)_2](ClO_4)$	ferric	6 N	NSLS X19A,10 K	7110.95(0.04)	0.5(0.1)	4.5(0.7)	1.8	0.11	88
				7112.70(0.01)	4.0(0.6)				
$[Fe(prpep)_2](ClO_4) \cdot 2CH_3OH \cdot CH_3CN$	ferric	6 N	SSRL 7-3,10 K	7110.96(0.03)	0.7(0.1)	6.4(0.9)	1.7	0.14	86
				7112.68(0.02)	4.5(0.2)				
				7114.44(0.35)	1.2(0.9)				
$K_3[Fe(CN)_6]$	ferric	6 C	SSRL 7-3,10 K	7110.09(0.01)	1.0(0.4)	5.2(0.2)	3.2	0.20	89
				7113.30(0.01)	4.1(0.2)				

[a] Pre-edge energies and intensities were determined by fits to the data (see the Experimental Section for details on the fitting procedure). [b] The values reported for the pre-edge intensities were multiplied by 100. [c] Peak energy differences are the energy differences between the first and second pre-edge features. [d] Peak intensity ratios are the intensity of the first pre-edge feature divided by the total pre-edge intensity intensity (all discrepencies are attributable to roundoff in the reporting of peak intensities).

Scheme 7

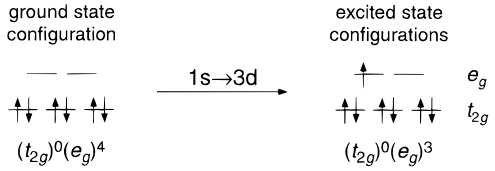

the higher energy feature is greatest in $K_3[Fe(CN)_6]$ (Table 3). A fit to the pre-edge region of $[Fe(prpep)_2](ClO_4)$ is shown in Figure 9B.

These low-spin ferric complexes all have octahedral iron site symmetry; thus, the 1s → 3d pre-edge feature may only gain intensity through the allowed electric quadrupole transition. The $^2T_{2g}$ ground state of an octahedral low-spin ferric complex has a $(t_{2g})^1(e_g)^4$ hole configuration, with two one-electron allowed excited configurations (Scheme 8).

The $(e_g)^4$ configuration gives an $^1A_{1g}$ excited state, while coupling of the holes in the $(t_{2g})^1(e_g)^3$ configuration produces $^1T_{1g}$, $^3T_{1g}$, $^1T_{2g}$, and $^3T_{2g}$ states. Energy splittings of the five states were calculated using a 10*Dq* value of 20 000 cm^{-1},[94] a *B* value of 1058 cm^{-1}, and a *C* value of 4500 cm^{-1}. The lowest energy state is the $^1A_{1g}$, with the $^3T_{1g}$ state being 0.9 eV higher in energy. The $^3T_{2g}$ state is 1.7 eV, the $^1T_{1g}$ state 2.2 eV, and the $^1T_{2g}$ 3.6 eV above the $^1A_{1g}$ state (Figure 9C). From comparison of these calculated energies to the fit of the $[Fe(prpep)_2](ClO_4)$ pre-edge region, it appears that the lower energy feature originates from a transition to the $^1A_{1g}$ $d^{(n+1)}$ final state, while the higher energy feature gains intensity from the $^3T_{1g}$, $^3T_{2g}$, and $^1T_{1g}$ states. The $^1T_{2g}$ state is highest in energy and appears as the weak high-energy shoulder.

Assuming that the feature at ~7112.7 eV contains the intensity from transitions in the $^3T_{1g}$, $^3T_{2g}$, and $^1T_{1g}$ states, the theoretical intensity ratio of the three pre-edge features should be 1:9:3. The fits to the $[Fe(prpep)_2](ClO_4)$ pre-edge region give an intensity ratio of 1:6.4:1.7. The discrepancy between the theoretical and observed intensity can be explained by covalency effects. The e_g set of orbitals is more covalent than the t_{2g} set due to σ bonding interactions with the ligands; therefore, the transition to the $^1A_{1g}$ state (the state associated with the $(t_{2g})^0(e_g)^4$ excited configuration) will have greater intensity than transitions to the T states (from the $(t_{2g})^1(e_g)^3$ excited configuration) which is consistent with the experimental data.

Energy splittings for the stronger field $K_3[Fe(CN)_6]$ complex (excited $10Dq = 28\,000$ cm^{-1})[94] were also calculated (Figure 9C, >10*Dq*). Again, the lower energy feature originates from a transition to the $^1A_{1g}$ state, while the higher energy feature gains intensity from transitions to the $^3T_{1g}$, $^3T_{2g}$, and $^1T_{1g}$ states.

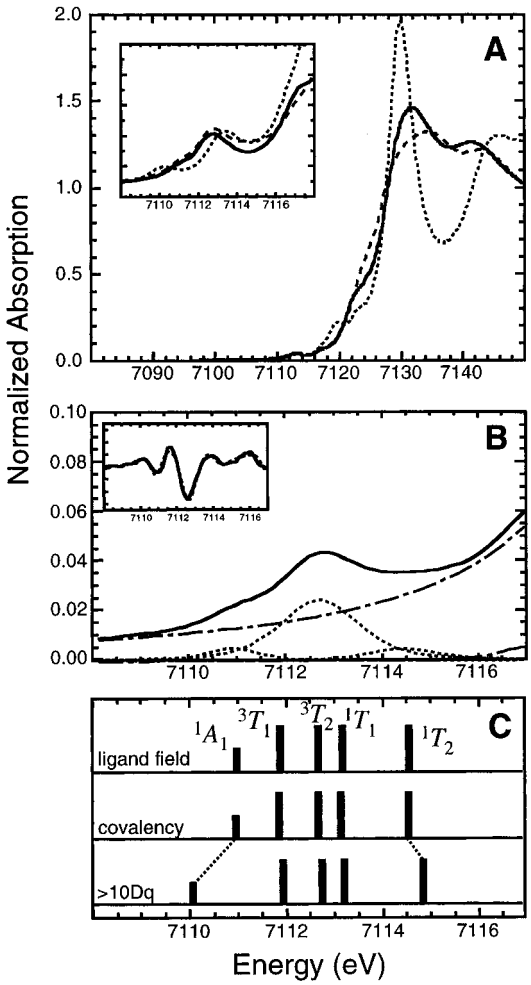

Figure 9. Fe K-edge XAS spectra, pre-edge fits, and theoretical analysis of octahedral low-spin Fe^{III} complexes. (A) Fe K-edge spectra of $[Fe(HB(pz)_3)_2](ClO_4)$ (—), $[Fe(prpep)_2](ClO_4)$ (- - -), and $K_3[Fe(CN)_6]$ (···) where the inset is an expansion of the 1s → 3d pre-edge region, with the normalized absorption scale being 0.0−0.1. (B) Fit to the Fe K-edge pre-edge region of $[Fe(prpep)_2](ClO_4)$ including the experimental data (—), a fit to the data (- - -), the background function (— -), and the individual pre-edge peaks from the fit (···). The inset displays the second derivative of the data (—) and the second derivative of the fit to the data (- - -). (C) Energy splitting and electric quadrupole intensity distribution of the $^1A_1$, $^3T_1$, $^3T_2$, $^1T_1$, and $^1T_2$ states and effect of changing covalency and increasing 10*Dq*.

The transition to the $^1T_{2g}$ state is at higher energy and should become unresolvable from the edge features. This is consistent with experiment as the high-energy peak needed to fit the energy

Scheme 8

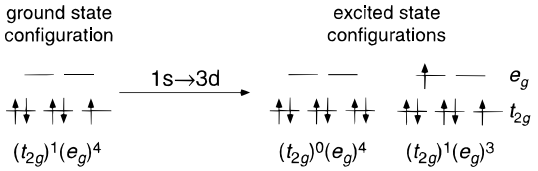

pre-edge region of $[Fe(prpep)_2](ClO_4)$ is not required to fit the data for the stronger field $[Fe(HB(pz)_3)_2](ClO_4)$ and $K_3[Fe(CN)_6]$ complexes.

Discussion

The 1s → 3d pre-edge region of Fe K-edge XAS spectra of iron complexes is sensitive to the electronic and geometric structure of the iron site. Although this general observation has been made previously, the present study presents a rigorous analysis of intensity, energy, and splitting of pre-edge features in a number of classes of iron complexes. Analysis based on free ion terms has been used to assign pre-edge features in XAS, yet it seems clear from this study that ligand field many-electron final states provide a more appropriate theoretical framework for the assignment and analysis of bound state, pre-edge features in iron complexes. The results presented above demonstrate that a combination of multiplet analysis and ligand field theory is an effective methodology for the analysis of Fe K-edge XAS pre-edge spectra. The combination of ligand field theory and DFT calculations is also shown to be effective at defining the distribution of Fe 4p character in the XAS final states.

Of general importance to XAS spectroscopy is the quantitative evaluation of intensity patterns and mechanisms for 1s → 3d transitions. As noted earlier, these transitions gain intensity via quadrupolar coupling or 3d−4p mixing. The electric dipole mechanism is only applicable where the iron site is in a noncentrosymmetric environment. Hence, in a centrosymmetric six-coordinate environment, intensity can only derive from the weak electric quadrupole mechanism. The distribution of this intensity over the pre-edge region depends upon the splitting of the spin-allowed many-electron final states, as determined by the oxidation and spin state of the metal atom. The intensity distribution can therefore be a sensitive probe of both in octahedral iron complexes. High-spin ferrous complexes in an O_h ligand field have three many-electron allowed $d^{(n+1)}$ final states ($^4T_{1g}$, $^4T_{2g}$, and $^4T_{1g}$). The higher energy $^4T_{1g}$ is easily resolvable at ∼2 eV above the two unresolvable lower-energy final states. This splitting increases with the strength of the octahedral ligand field, an observation which cannot be explained on the basis of free ion terms alone. High-spin octahedral ferric complexes have two allowed final states ($^5T_{2g}$ and ^5E_g) split by the excited state 10*Dq* of the complex. From this study, the magnitude of 10*Dq* in an XAS excited state is found to be ∼80% of the ground state value. The reduction in 10*Dq* splitting is consistent with observations from optical spectroscopy which show a significant reduction of 10*Dq* in charge-transfer excited states. The decrease in 10*Dq* is less pronounced in K-edge XAS spectroscopy because of the increase in effective nuclear charge associated with the 1s core hole. The two final states are also split by ∼2 eV for most of these ferric complexes. The ferric pre-edge features are centered at ∼1 eV higher energy (∼7113.5 eV) than their high-spin ferrous counterparts (∼7112.5 eV). In the low-spin ($S = 0$) state, octahedral ferrous complexes have only one accessible one-electron allowed XAS final state (^2E_g) and thus only exhibit one peak in the pre-edge region. This peak is observed at ∼7112 eV with nitrogen ligation. Conversely, low-spin ferric complexes have a large number of one-electron allowed final states ($^1A_{1g}$, $^1T_{1g}$, $^3T_{1g}$, $^1T_{2g}$, and $^3T_{2g}$) and have a relatively complex intensity distribution. Experimentally, the $^1A_{1g}$ final state is at lower energy (∼7110 eV) and is observed as a shoulder to the higher intensity peak containing contributions from the $^1T_{1g}$, $^3T_{1g}$, $^1T_{2g}$, and $^3T_{2g}$ final states. In each case, centrosymmetric octahedral iron complexes have very weak pre-edge features with intensity distributions characteristic of oxidation and spin state. The ferric complexes tend to have somewhat greater total pre-edge intensities than their ferrous counterparts, consistent with the additional hole present in the ground state.

The 1s → 3d pre-edge feature is also sensitive to the geometry of the iron site as noncentrosymmetric distortions allow for 3d−4p mixing, thereby increasing the intensity of the pre-edge feature. Specifically, one can consider the effects of axial distortions upon complexes with O_h symmetry. Distortions that do not break the inversion symmetry at the metal ion (such as a D_{4h} distortion) will affect the distribution of the electric quadrupole intensity but should not affect the total intensity of the pre-edge region. However, breaking the centrosymmetry can have dramatic effects on both the total intensity and the intensity distribution of the 1s → 3d pre-edge feature. Two experimental cases of axial C_{4v} distortions are six-coordinate oxo-bridged dimers (one short axial bond, strong field distortion) and five-coordinate C_{4v} monomers (loss of one axial ligand, weak field distortion). In both cases, the intensity distribution is understood by invoking 3d−4p mixing into the orbital component along the distortion. The inversion symmetry is broken along the *z*-axis of the complex and allows strong mixing between the $3d_{z^2}$ and the $4p_z$ orbitals (both of a_1 symmetry). Although the $3d_{xz,yz}$ and $4p_{x,y}$ orbitals are allowed to mix by group theory, XAS data and molecular orbital calculations demonstrate that negligible mixing occurs in the *x, y* plane.

DFT calculations have been used to investigate the effect of strong field and weak field distortions on the 1s → 3d pre-edge feature for both ferrous and ferric complexes. These results are summarized in Figure 10. The final state associated with the one-electron transition to the Fe $3d_{z^2}$ orbital is most affected by axial distortions. The weak field distortion causes splitting of the 3d orbitals and stabilizes the Fe $3d_{z^2}$ orbital, lowering the energy of the pre-edge transition into that orbital. In concert, $4p_z$ mixing into the $3d_{z^2}$ orbital increases with the distortion. The effect of a strong field C_{4v} distortion is similar. The 3d orbitals split due to the lowering of the symmetry, but in this case, the $3d_{z^2}$ orbital energy increases as a result of the stronger ligand field along the *z*-axis. The intensity of the state associated with the transition to the $3d_{z^2}$ will again increase due to $4p_z$ mixing. The DFT-calculated amount of $4p_z$ mixing into the $3d_{z^2}$ orbital due to a C_{4v} distortion is shown in Figure 11 for $FeCl_6^{3-}$ as a model. Similar results are obtained for ferrous systems. In both oxidation states, the increase in 4p mixing at short distance (*i.e.*, for strong field C_{4v} distortions) is very pronounced, implying that 4p mixing should be highly sensitive to bond length changes in six-coordinate complexes with one short (*i.e.*, Fe═O) bond distance.

For five-coordinate complexes, the pre-edge feature is also sensitive to geometric and electronic factors. High-spin ferrous C_{4v} complexes have three one-electron allowed final states (^4E, $^4B_2$, and $^4A_2$) while equivalent ferric complexes have four final states ($^5B_2$, ^5E, $^5A_1$, and $^5B_1$). Experimentally, each has an intense low-energy peak with a much weaker peak at higher energy (Figures 3 and 6). In both cases, the highest energy final state is associated with the 1s → $3d_{x^2-y^2}$ transition and the low-energy feature is dominated by the electric dipole-enhanced 1s → $3d_{z^2}$ ($+4p_z$) transition. The greater effective nuclear charge in the ferric sites is reflected in the higher energy of the pre-

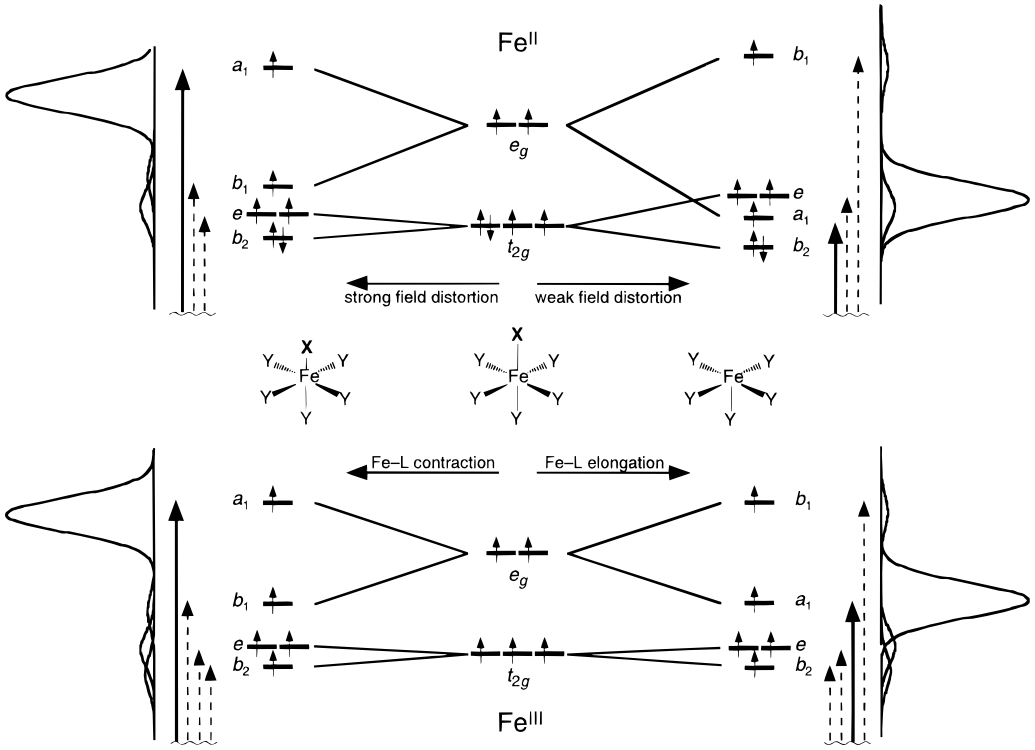

Figure 10. Qualitative molecular orbital analysis based upon density functional final state calculations. Ferrous (top) and ferric (bottom) complexes are distorted from an idealized octahedral geometry (center) along one axis. The Fe−X bond is contracted going toward the left and is elongated toward the right. Semiquantitative one-electron orbital configurations (based on final state calculations) are shown for each geometry. A simulation of the pre-edge region is also shown.

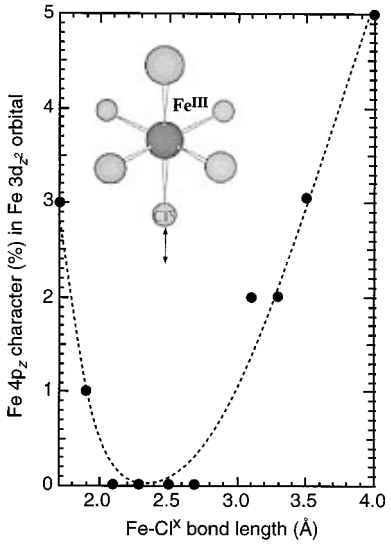

Figure 11. Amount of $4p_z$ mixing into the $3d_{z^2}$ orbital as a function of axial distortion in $[FeCl_6]^{3-}$ as calculated using DFT calculations; only the Fe−Cl^X bond distance is varied. Points represent the calculated $4p_z$ character in the ferric model, while the dashed line represents a polynomial fit to these points.

edge features relative to the ferrous complexes. A five-coordinate geometry that we have not investigated experimentally is the trigonal bipyramidal geometry (D_{3h} symmetry). Molecular orbital calculations on models for this geometry indicate that (i) the total intensity of the D_{3h} pre-edge feature should be similar to that observed in C_{4v} complexes and (ii) the electric dipole intensity should distribute into final states that involve transitions into orbitals along the equatorial plane. Just as in the C_{4v} complexes, 3d−4p mixing will only be important in directions where centrosymmetry is broken. The trigonal bipyramidal geometry enforces centrosymmetry along the *z*-axis while breaking it in the equatorial plane and allows $4p_{x,y}$ mixing into the $3d_{xy,x^2-y^2}$ orbitals. Overall, a geometric transformation from C_{4v} to D_{3h} symmetry in five-coordinate complexes causes a redistribution of the electric dipole intensity from the C_{4v} axial direction to the D_{3h} equatorial plane and thus from the final state associated with the $3d_{z^2}$ to the $3d_{x^2-y^2,xy}$ orbitals. Experimentally, this should be observed as a shift in intensity to higher energy states in D_{3h} symmetry.

Elimination of a ligand on going to four-coordination generally leads to a further increase in total pre-edge intensity. The intensity of the pre-edge features of tetrahedral complexes can be attributed to loss of centrosymmetry along the *x*, *y*, and *z* coordinates and consequently a large electric dipole component from 3d−4p mixing. Ferrous T_d complexes have been calculated to have four final states that contribute to the pre-edge region ($^4A_2$, $^4T_2$, and two $^4T_1$), although one of these is formally a two-electron forbidden XAS final state (the higher energy $^4T_1$). The orbital splitting in T_d complexes is not expected to be large enough to be resolvable at the XAS pre-edge, but configurational interaction distributes intensity into the higher energy feature which is ∼2 eV higher in energy. In the ferric case, the two final states (^5E and $^5T_2$) are split by an excited state $10Dq$ which cannot be resolved, giving one broad feature in the pre-edge.

From the analysis of experimental data from a large number of iron model complexes, it has thus been found that the Fe K-edge XAS pre-edge region can be used to obtain detailed information about the oxidation and spin state as well as the site geometry of iron. It has been previously noted that the total intensity of the pre-edge region could be directly correlated with the coordination number of an iron complex.[1,21] However, the present investigations suggest that total intensity alone may not be sufficient to adequately assign site geometry and coordination number. For example, [Fe(TMC)Cl](BF$_4$), a five-coordinate ferrous complex, and $(Et_4N)_2[FeCl_4]$, a four-coordinate ferrous complex, have the same total pre-edge intensity of 12.9. On the basis of total intensity alone, these compounds would be indistinguishable; however, the distribution

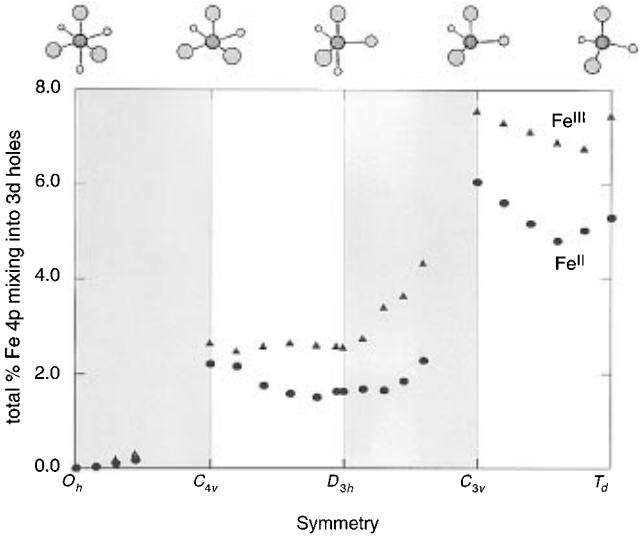

Figure 12. Calculated total 4p mixing into XAS final states for a series of geometries from O_h to T_d. Results shown are for a series of ferrous (●) and ferric (▲) geometry-optimized structures with chloride ligation. Idealized geometries are shown above.

of the intensity in these complexes is very different. [Fe(TMC)Cl](BF$_4$) has an intense pre-edge feature at 7111.4 eV with an extremely weak feature at 7113.4 eV (Figure 3), while (Et$_4$N)$_2$[FeCl$_4$] has two intense peaks at 7111.6 and 7113.1 eV (Figure 2). In the T_d case, the electric dipole intensity (from 4p mixing into the 3d orbitals of t_2 symmetry) is distributed over both pre-edge features (Figure 2), while in the C_{4v} case, the electric dipole intensity from 4p$_z$ mixing into the 3d$_{z^2}$ orbital is located only in the lowest energy pre-edge feature (Figure 3). From this example, it is clear that intensity distributions can be very important in the analysis of pre-edge features.

DFT calculations on a series of iron chloride models ranging from O_h to T_d symmetry have been performed to simulate a geometric progression for common ferrous and ferric geometries. These calculations, although not necessarily quantitative in determining mixing values, yield valuable information in defining trends in both the total amount of 4p character and its distribution over the Fe 3d orbitals over this limited series. The results are summarized in Figure 12, which demonstrates several key features of the influence of geometry on 4p mixing into Fe 3d orbitals. Two clear trends are observed from these calculations: (i) the amount of 4p mixing into the 3d orbitals is consistently greater for ferric *vs* ferrous complexes and (ii) the loss of a ligand increases the amount of total 4p mixing. The increased 3d-4p mixing in ferric complexes is attributable to the generally shorter bond lengths in such complexes, thereby accentuating geometric perturbations. The removal of a ligand greatly perturbs the symmetry of a site and will generally cause a break in centrosymmetry along one axis of a complex. Geometric transformations from O_h to C_{4v} and from D_{3h} to C_{3v} both involve the removal of a ligand along a centrosymmetric axis (z-axis) which will greatly increase mixing of the 4p$_z$ orbitals with 3d$_{z^2}$. Shorter bonds in the lower coordination complexes will also contribute to the increase in 4p mixing. As described previously, simple geometric reorganizations will have only small effects on the total amount of 4p mixing into the Fe 3d orbitals.

A critical conclusion of this study is that although there is a general trend which supports the correlation between total Fe K-edge pre-edge intensities and coordination number at the Fe site, this relationship must be used with caution. The relationship fails under circumstances where complexes exhibit strong distortions from optimal geometries and/or have very different ligation. This should be true for both ferrous and ferric complexes, although the former are more likely to deviate from the simple intensity correlation since they are not as sensitive to coordination number (see Figure 12). However, a detailed analysis of both the total intensity and the intensity distribution of the pre-edge features has been found to be an accurate method of understanding both geometric and electronic structural features of iron complexes. Analysis of energy splittings and intensity distribution in the 1s → 3d pre-edge feature are useful in the elucidation of both the coordination number and geometry of iron sites. In addition, the multiplet structure of the pre-edge feature is specific for a given oxidation and spin state of an iron atom. In combination with information from other regions of the Fe K-edge XAS spectrum (EXAFS and edge analysis), the pre-edge region is an important tool for elucidating the electronic environment of iron complexes. These systematics should be of particular use in studying the electronic structure of Fe sites in metalloproteins as a function of oxidation state and intermediates along reaction paths.

Acknowledgment. Professors Richard H. Holm, Nobumasa Kitajima, Stephen J. Lippard, and Pradip K. Mascharak and the Smithsonian Institute are thanked for providing some of the model complexes in this study. Dr. A. Lawrence Roe is thanked for measuring the data on the [Fe(TMC)X](BF$_4$) series. This research is supported by grants from the NIH (GM40392, E.I.S.) and NSF (CHE-9423181, K.O.H.). Support is provided to P.K. by the Natural Sciences and Engineering Research Council (Canada) in the form of a 1967 Science & Engineering Scholarship. The computer used for XAS analysis was obtained through NSF Grant CHE-9408185. The data were collected at the Stanford Synchrotron Radiation Laboratory and the National Synchrotron Light Source, Brookhaven National Laboratory, which are supported by the U.S. Department of Energy, Office of Basic Energy Science, Divisions of Chemical and Materials Sciences. SSRL is also supported in part by the National Institutes of Health, Biomedical Technology Program (Grant RR-01209), and the U.S. Department of Energy, Office of Health and Environmental Research.

JA964352A